UCRL 50016-76-3

MECHANICAL ENGINEERING DEPARTMENT QUARTERLY REPORT

July through September 1976

September 30, 1976

Prepared for U.S. Energy Research & Development Administration under contract No. W-7405-Eng-48

LAWRENCE LIVERMORE LABORATORY
University of California/Livermore

DISCLAIMER

Printed in the United States of America
Available from
National Technical Information Service
U.S. Department of Commerce
5285 Port Royal Road
Springfield, VA 22161
Price: Printed Copy $; Microfiche $2.25

Page Range	Domestic Price	Page Range	Domestic Price
001–025	$ 3.50	326–350	10.00
026–050	4.00	351–375	10.50
051–075	4.50	376–400	10.75
076–100	5.00	401–425	11.00
101–125	5.50	426–450	11.75
126–150	6.00	451–475	12.00
151–175	6.75	476–500	12.50
176–200	7.50	501–525	12.75
201–225	7.75	526–550	13.00
226–250	8.00	551–575	13.50
251–275	9.00	576–600	13.75
276–300	9.25	601–up	*
301–325	9.75		

*Add $2.50 for each additional 100 page increment from 601 to 1,000 pages: add $4.50 for each additional 100 page increment over 1,000 pages.

LAWRENCE LIVERMORE LABORATORY
University of California/Livermore, California/94550

UCRL 50016-76-3

MECHANICAL ENGINEERING DEPARTMENT QUARTERLY REPORT

July through September 1976

Scientific Editor: R.G. Stone
General Editor: M.B. Bathgate

MS. date: September 30, 1976

Contents

DOUBLE-EXPOSURE HOLOGRAPHIC INTERFEROMETRY USING COMMON-PATH REFERENCE WAVES

In optical and nondestructive testing, it is often necessary to make measurements with more accuracy than the current testing methods are capable of attaining. This is the case when the wavefront distortion of high-quality plano-optics is less than a wavelength of light or the deformation of the object is tens or hundreds of Angstroms. To extend our measurement capability, we have developed a variation of double-exposure holographic interferometry that yields high-accuracy measurements. This is accomplished by the use of two unique optical components: a reference-wave generator that produces two common-path, orthogonally polarized, diffuse reference waves; and an optical phase shifter that varies the relative phase of the reference waves in small increments to provide high resolution.* These components are incorporated into a typical holographic arrangement.

New Optical Components

Reference-Wave Generator. The reference-wave generator is composed of three elements (a Wollaston prism, a microscope objective, and a ground-glass screen), as shown in Fig. 1. The horizontal and vertical components of polarization are transmitted by the Wollaston prism with a slight angular divergence. They are focused with a microscope objective to produce two point sources with a separation of approximately 60 μm. The sources illuminate a ground-glass screen that generates two orthogonally polarized diffuse waves of the photographic plate which act as reference waves. The small but finite separation of the point sources introduces a slight optical path difference to points on the ground-glass screen and thus, the reference waves are uncorrelated. As will be shown later, this is essential for proper reconstruction of the hologram. By controlling the state of polarization of the incident wave, either or both of the reference waves can be generated. This is particularly important in the recording and reconstructing steps (described below in the experimental section).

Optical Phase Shifter. The optical phase shifter is used during reconstruction to control the relative phase of the reference waves. This component consists of a half-wave plate mounted in the hollow shaft of a stepping motor, followed by a stationary quarter-wave plate (see Fig. 1). When the horizontally polarized wave from the laser passes through the half-wave plate, oriented with its fast axis (F) at angle θ to the x-axis, the linear polarization is rotated by 2θ. This wave can also be thought of as the linear combination of two waves of opposite circular polarization with a relative phase difference of 4θ. After the waves pass through the quarter-wave plate they are transformed to horizontally and vertically polarized waves, preserving the phase difference. Thus we see that, by changing θ, the relative phase of the two orthogonally polarized waves can be controlled. For a stepping motor with 2000 steps per revolution, the relative phase can be changed in increments as small as $2\pi/500$.

Experimental Procedure and Analysis

The procedure for recording and reconstructing a double-exposure hologram is slightly different from the normal procedure because it depends on the state of polarization in the optical system. The analysis also differs due to the nature of the reference waves.

Recording the Hologram. The optical system for recording the hologram is shown in Fig. 1 (top). By rotating the half-wave plate to the proper angle, any orientation of linear polarization may be introduced into the optical system. To record the double-exposure hologram, the half-wave plate is set for horizontal polarization. This ensures that only one reference wave is generated. An exposure is made of the object in the initial state. Then, while the object is undergoing a change, the half-wave plate is rotated 45° by the stepping motor. This produces vertical polarization and generates the other reference wave. A second exposure is made of the object in its final state. The photographic plate is then removed and processed.

Reconstructing the Hologram. After processing, the photographic plate must be replaced in its holder with a positioning error of less than the characteristic speckle size produced by the ground-glass screen. This is determined by the angular subtense of the ground-glass screen as seen from a point on the plate (approximately 2 μm for this system). The optical system for reconstruction is illustrated in Fig. 1 (bottom). Because the optical phase shifter produces horizontal and vertical polarizations simultaneously, two reconstruction waves are generated, which have the same complex amplitude as the reference waves. Since these waves have spatially random phases, which are uncorrelated, only the waves associated with the primary images of the object in its initial and final

*In this paper the term resolution refers to the smallest measurable change of a quantity and the term accuracy refers to the agreement between the true value of a quantity and its measured value.

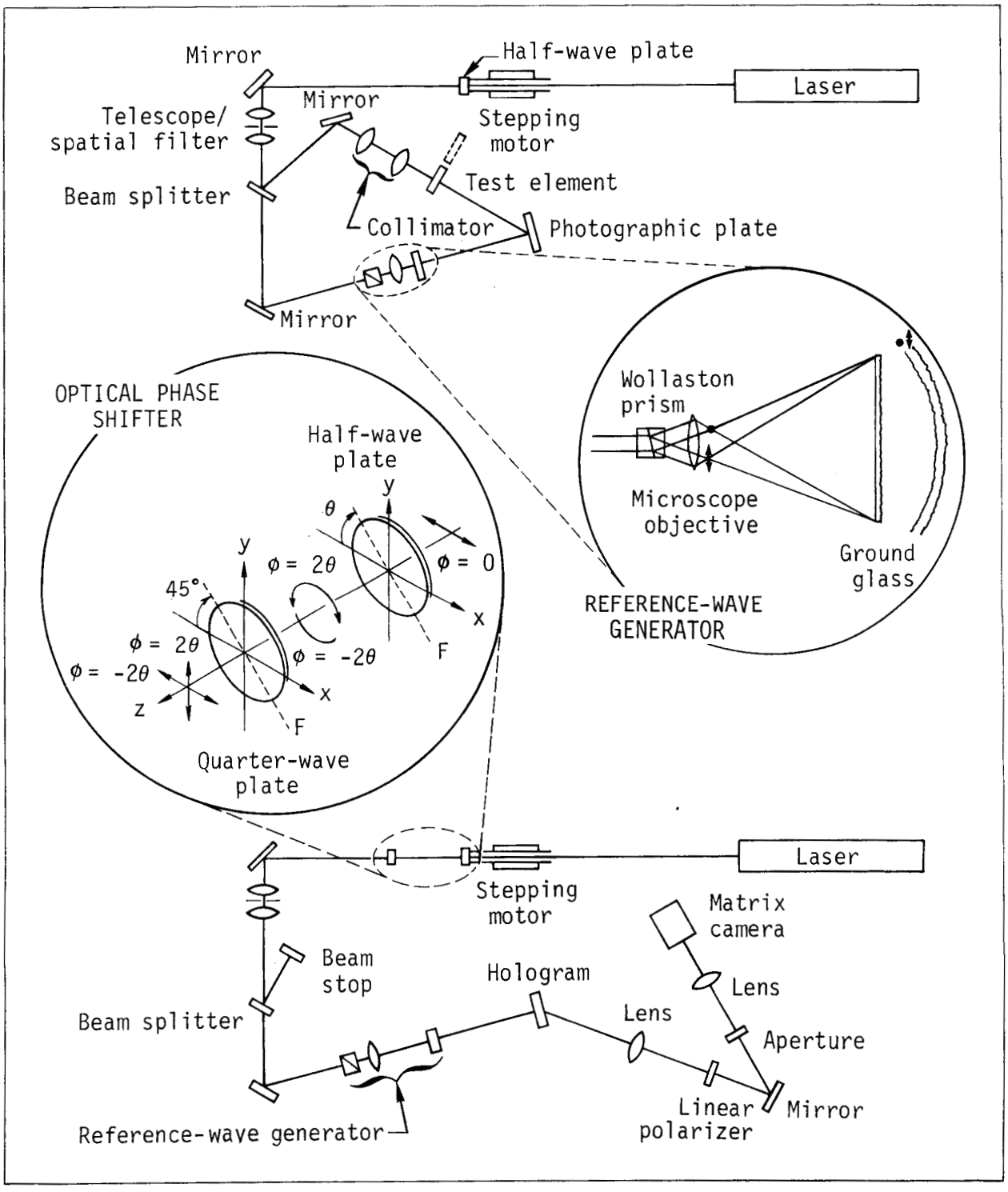

Fig. 1. Experimental setup for recording (top) and reconstructing (bottom) the double-exposure hologram. The two unique components distinguishing this setup from conventional holographic interferometry are shown in the two insets: a polarization-dependent common-path reference-wave generator (right) and an optical phase shifter (left). In the reference-wave generator, the input waves vertical (dot) and horizontal (arrow) components are transmitted by a Wollaston prism and microscope objective onto a ground-glass screen, which generates the two uncorrelated, orthogonally polarized diffuse waves used to record and reconstruct the hologram. The optical phase shifter allows precise control of the relative phase ($\Delta\phi$) between the two reference waves used in reconstruction. The laser input wave to the optical phase shifter is linearly polarized in the horizontal direction; the output is two waves orthogonally polarized in the horizontal and vertical directions with a phase difference of 4θ.

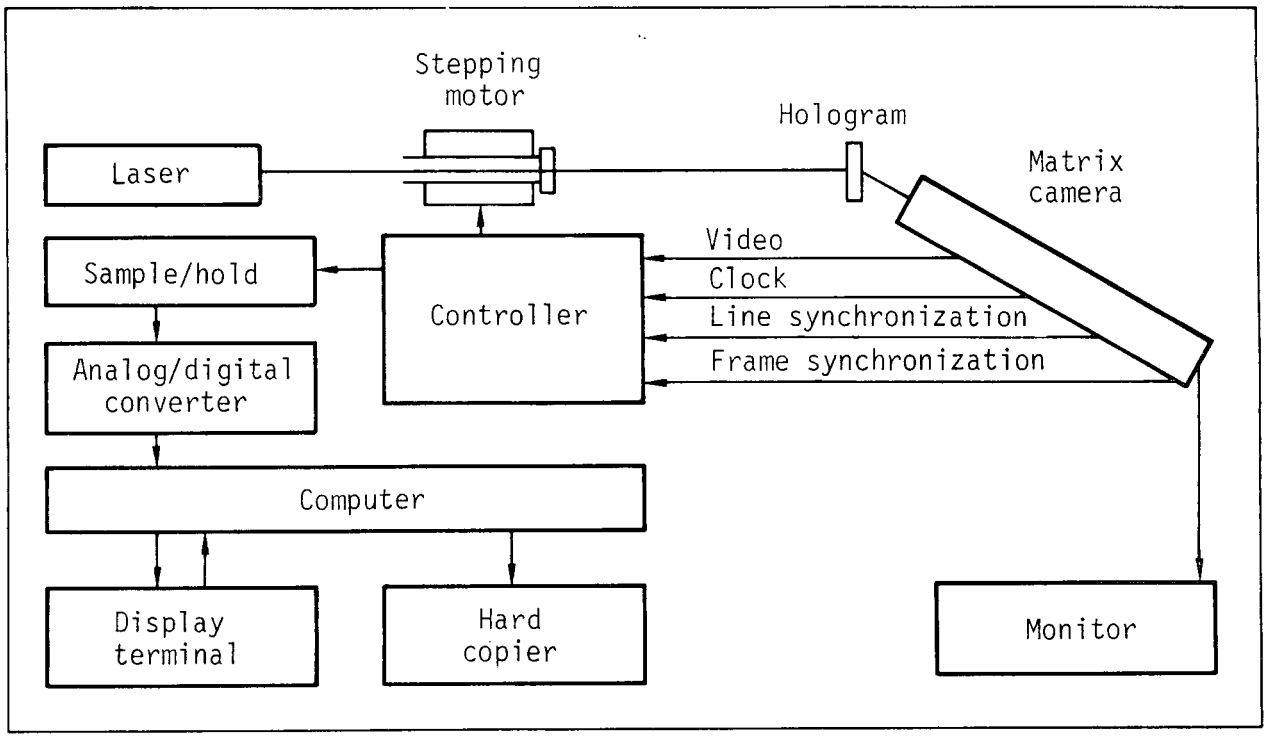

Fig. 2. System for data acquisition, analysis, and display.

states are reconstructed. The waves associated with the conjugate and cross-talk images appear as diffuse waves.

When the waves associated with the primary images are brought to focus with a lens, it is necessary to pass them through a linear polarizer with its axis bisecting the horizontal and vertical polarizations. The polarizer causes the images to interfere, forming an interferogram. The diffuse waves produce a speckle pattern background resulting from rapidly varying phases.

Analysis of Interferogram

The irradiance of the interferogram has the same form as that for conventional double-exposure holographic interferometry except that it is a function of the optical-phase shifter parameter, θ. By varying this parameter in a controlled manner, the phase of the interferogram can be determined with high resolution by synchronous detection.[1]

System Operation. The coupling of the optical system to a computer system is shown in Fig. 2. The interferogram is detected by a self-scanned matrix camera with a 32 X 32 photodiode array, free running at about 50 ms per frame. The video signal, along with clock, end-of-line, and end-of-frame synchronization pulses, is sent to a controller that operates on a three-frame cycle. The first frame is the data frame where the video signal is sent through a sample/hold circuit and an analogue/digital converter to the computer. At the beginning of the second frame, the stepping motor changes θ by $2\pi/N$, where N is the number of steps per revolution. The third frame clears the photodiode array in preparation for the next cycle. During the second and third frames, the computer updates the necessary calculations, so that it is never necessary to store more than one data frame at any given time. The process continues until N/4 data frames are read into the computer. The value of N can be as large as 2000 but, for most measurements, N is set at 200 for a total of 50 data frames. Less than ten seconds are required for data acquisition and computation of the phase.

Graphic Displays. Before plots representing the change in the object between its initial and final states can be displayed, it is necessary to define the boundary of the object and to remove 2π discontinuities in the phase.

The boundary (if one exists) is defined by first calculating the modulation amplitude of each photodiode in the array. Points outside the boundary of the object have a much smaller modulation amplitude than do points inside. A distribution plot of the number of photodiodes with a given modulation

amplitude is displayed on the terminal screen. The cut-off amplitude is determined by the operator by setting a cursor on the screen. This defines the boundary. Points inside the boundary are searched for 2π discontinuities and are corrected until the phase over the entire object is continuous. Finally, the phase at the center photodiode position is subtracted from all positions so that the center is at phase zero and serves as a reference point.

To assist the operator, the extreme values of the phase are displayed. After an appropriate contour interval is keyed in, a contour plot is displayed. For better physical understanding of the contour plot and to distinguish maxima from minima, a perspective plot is also displayed with a reference height appearing in the lower left corner. The operator can specify the desired viewing direction and angle. Hard copies of these plots can be made at this time.

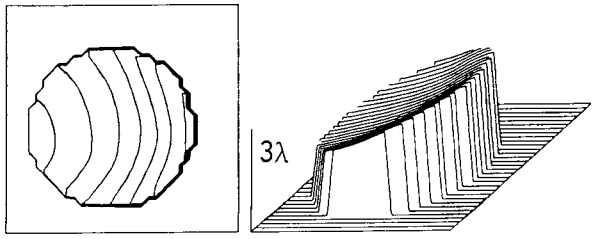

Contour interval = λ/5

(a)

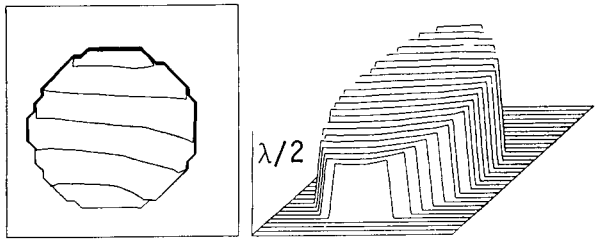

Contour interval = λ/20

(b)

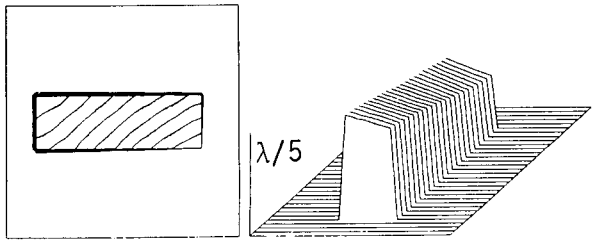

Contour interval = λ/100

(c)

Fig. 3. Contour and perspective plots (a and b) of two glass disks of different optical quality, and (c) of a thermally distorted steel plate.

Experiments

This variation of double-exposure holographic interferometry is intended for accurate measurements when the difference between the initial and final states of the object is on the order of one wavelength or less. For demonstration purposes, this technique was applied to two areas of interest, optical and nondestructive testing.

Optical Testing. This technique is well suited for measuring the wavefront distortion introduced by plano-optical elements or systems (e.g., substrates for windows and beamsplitters, laser and Faraday rotator disks, entire laser amplifiers) because it is possible to compare the wavefronts passing through the test element and the air space occupied by the element.

The test object was a glass disk. The initial exposure was made with the disk in a collimated wave and the final exposure was made with the disk moved out of the beam. Double-exposure holograms of several disks of varying optical quality were made. The contour and perspective plots of two of these disks are shown in Fig. 3a and b (note difference in scale). Further analysis of this data yields the tilt, the root-mean-squared wavefront error, and the symmetric aberrations.

Nondestructive Testing. Since holographic interferometry allows comparison of the initial and final states of an arbitrarily shaped object, it is especially useful in nondestructive testing. To test our technique's effectiveness in this area, we used it to measure thermal distortion in a steel plate. The experimental arrangement was similar to that shown in Fig. 1. The initial exposure was made with the plate in thermal equilibrium and the final exposure was made after one corner of the plate was cooled. The contour and perspective plots are shown in Fig. 3c. Although the contour interval is λ/100, the corresponding physical distortion is even less (the actual value depends on the geometry of the optical arrangement). The total distortion over the entire plate is about λ/10, too small to produce fringes in a conventional holographic interferometer.

Accuracy and Sources of Error

In general, contour plots can be produced with high resolution (small contour intervals), but they do not

necessarily have physical significance. Errors inherent to the specific measurement limit the accuracy that can ultimately be achieved. Therefore, it is essential that the accuracy of this technique be determined so that the data can be properly interpreted.

The accuracy was determined experimentally with the same optical arrangement used for the wavefront distortion measurements except that in this case, the object wave (i.e., the collimating lens used as the object) was compared with itself. Two different measurements were made to distinguish between the sources of error and their relative contributions.

The first measurement was made without a hologram. Instead of reconstructing the two object waves, the reference waves were blocked and the actual object waves were used. Theoretically, the values of the phase at each point should be equal. However, sources of error were introduced by the phase shifter, optical system, air turbulence during data acquisition, matrix camera, computer, and associated interfaces. These combined components limit the accuracy to about $\lambda/500$ over the entire field of the photodiode array.

The second measurement was made by recording a double-exposure hologram of the object waves. In addition to the errors present in the first measurement, errors were introduced by air turbulence between the two exposures and by processing and replacement of the photographic plate. Other holograms were made with the same optical arrangement and these gave different contour plots with the same number of contours, indicating the random nature of the errors. From these results, it was concluded that the sources of error associated with the holographic process limit the accuracy to about $\lambda/100$ over the entire field.

Summary

We have described a variation of double-exposure holographic interferometry that achieves high accuracy by the use of a unique reference-wave generator and an optical phase shifter. This type of interferometry is particularly useful when changes between the initial and final states of the object are approximately one wavelength or less. Measurements of the inherent error indicate that a precision of $\lambda/100$ over the field of view can be attained.

TEMPERATURE MEASUREMENTS IN AND AROUND AN ELECTRON-BEAM WELD CAVITY DURING WELDING

Electron beam (EB) welding is useful in joining parts in weapons. It gives deep penetration with minimum melting of material, which results in less distortion in the welded product. Successful EB welds are presently obtained by many weld trials combined with EB weld experience. Although much effort has been expended, definition of the EB welding process remains elusive and its behavior mysterious. Extensive studies of the effects of such factors as beam current, power, focus current, and part motion have not been successful in explaining the process. Thus, it is not possible to specify values to use for welding in new materials or under changed conditions. To better understand this process, and hopefully, to establish some parameters, we have measured the molten metal temperatures in and around the EB cavity during welding.

Background

In EB welding, materials are fusion-joined by the bombardment of the interface region with a well-defined stream of high-energy electrons. The welding is usually done in a vacuum chamber at pressures on the order of 1 mPa. Since electrons are capable of penetrating only a very short distance into the material surface, the EB energy is absorbed in a very thin layer of material, causing it to melt and some to vaporize. The resulting vapor pressure pushes the liquid aside, which causes a small cavity to form and exposes more solid material. In this manner the EB is able to deposit its energy substantially below the surface of the workpiece.

To use the electron beam for welding purposes, it must be focused at or near the workpiece surface. During this focusing process, due to imperfect electron optics, the beam current distribution distorts gradually as the degree of focusing is increased. A beam focused to an elongated spot has different fusion-zone features depending on the direction of the weld pass. To avoid this, it would seem advantageous to use a small and highly concentrated beam, which produces larger depth-to-width ratios. However, actual experience indicates that such beams are conducive to the formation of welding defects such as porosity, cold shuts, or spiking.

Equally important to successful EB welding is the actual distribution of energy in the beam. Measurements of the distribution at low energy display a ragged appearance with many localized energy peaks. At higher power levels one might expect large differences in energy density throughout the beam.

Furthermore, these localized peaks in the energy distribution vary with time and are possibly even more accentuated that those at lower power levels. Therefore, even for a beam that is not highly focused, the potential exists for spiking if a localized peak occurs with an extremely high energy density for a sufficient duration.

No detailed physical explanation of the EB interaction with the material surface exists. However, one model is that the metal vapor pressure maintains an open cavity that is surrounded by the liquid metal. Due to the liquid hydrostatic head, this metal periodically flows into the cavity. At the same time, the surface tension constricts the cavity and also pulls some molten metal to the cavity top. It is generally believed that the interaction of these forces allows deep penetration. It appears that for significant EB cavity penetration the local vapor pressure must be greater than the sum of the forces due to surface tension and hydrostatic head.

Using the above model, we have estimated that producing a 3-cm-deep, 0.13-cm-diameter hole in aluminum with an EB welder requires a vapor pressure of about 3.3 kPa. From the known vapor pressure-temperature relationship we then determined the surface temperature to be 1900°C. As mentioned above, a highly focused EB or a beam with non-uniform energy distribution could produce a slightly higher metal temperature at the base of the cavity. Such a temperature change of only a few hundred degrees could produce a dramatic change in the local vapor pressure that might lead to momentary deeper penetration (spiking phenomenon).

If we could determine temperatures in the weld cavity, we could validify the proposed model. This could provide a clearer understanding of the EB weld process, and ultimately might lead to improved EB weld development. However, measuring the molten metal temperature in the weld cavity is very difficult. Measurements of the molten pool temperature near the cavity are easier to obtain and may be useful in predicting perturbations in the cavity.

Experiments

Our technique for making such a measurement is to use an infrared detector to sense radiation given off by the molten weld pool. For such a measurement to be possible, the infrared device must be able to sense radiation from a small spot. The size of this spot must be 0.1-0.8 mm in diameter so that a local temperature measurement can be obtained. An optical fiber system with a focusing lens has been purchased that provides the desired spot size (~0.5 mm). The radiation is transmitted through this fiber bundle to a photo multiplier and then to the infrared detector. The location of the temperature measurement in the material surface plane can be controlled manually from outside the EB chamber during welding. Although the description is relatively simple, much hardware design was required to produce a successful reading.

All weld studies have been conducted on the Sciaky EB welder located in Building 321, Room 1317. It is a low-voltage high-current welder (30 kV, 500 mA limits) and has automatic control features. We have made temperature measurements in the molten pool and cavity during welding of several aluminum alloys, several stainless steel alloys, and pure tantalum. Table 1 lists representative temperature data for the materials welded. These measurements have been obtained for various EB parameters such as power, focus, and weld speed.

Table 1. Range of maximum temperatures of molten metal in cavity during EB welding

Material	Maximum cavity temperatures (°C)
1100 aluminum	1680 → 1900
5083 aluminum	1100 → 1290
6061 aluminum	1650 → 1850
7075 aluminum	1000 → 1200
Hy-180 steel	1800 → 1960
20-6-9 steel	1600 → 1670
304 St steel	1760 → 1880
Tantalum	4160 → 4600

Since all materials were solid plate, the weld studies do not represent joining of two separate plates. The test sequence on the aluminum alloys consisted of a continuous weld through four 90° pie-shaped pieces with the same EB machine settings. The maximum temperature readings were different for each alloy.

An accurate temperature measurement depends on knowing the surface emissivity. The emissivity during weld conditions was determined by recording the infrared detector response from molten metal in the EB chamber immediately after the power was shut off. As the metal solidifies, the melt temperature and the detector response remain constant. For a known melt temperature, one can then determine the emissivity at melt. Emissivity at higher temperatures are obtained based on the observation (and theoretical support) that the emissivity increases linearly with temperature. The values measured for the test materials average ~0.3 for the steels and ~0.1 for the aluminum and tantalum. Using the surface emissivity, we converted the infrared

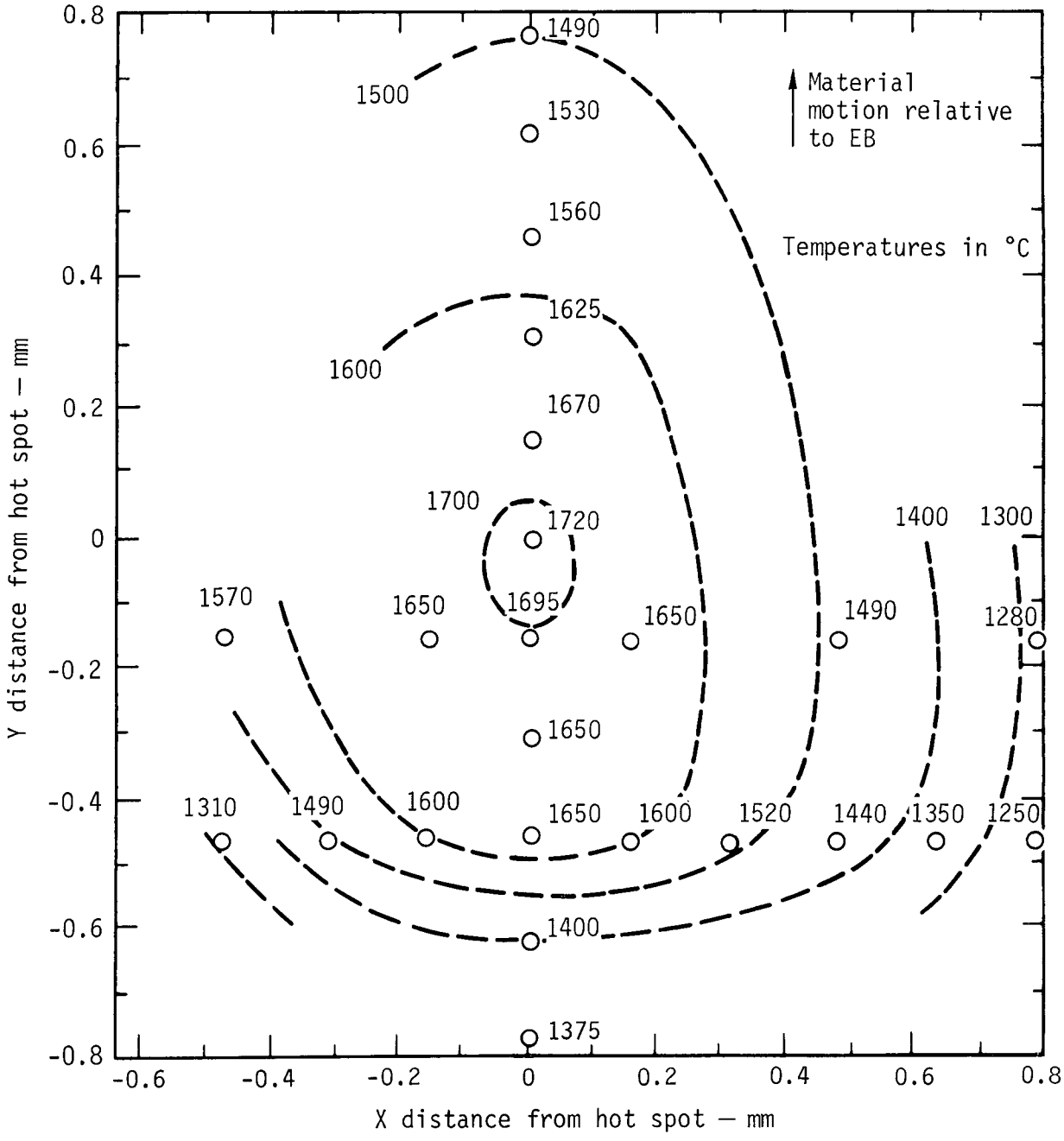

Fig. 4. Measured molten metal temperature in and around the EB cavity during 10 min of continuous welding on a 30.5-cm-diameter 1100-aluminum plate (14-kV beam voltage, 125-mA beam current, 2.5-cm/s weld speed).

measurements of the molten metal in the cavity during welding to temperature.

Figure 4 shows a contour temperature plot for 1100 aluminum. This data was obtained during a 10-min weld (~20 revolutions). The temperature gradient behind the weld is much less severe than that to the side or ahead of the weld. Figure 5 displays the temperature measurement and the fusion line (from weld section) for a one-pass weld in 1100 aluminum. There is good correlation between the fusion width (~0.5 cm) and the width defined by the low temperature readings (~0.64 cm). In regions of a steep temperature gradient, the temperature is an average of the temperatures in the 0.5-mm-dameter measurement area. Thus a reading of 1000°C could actually result from a spot having temperature extremes of 820 to 1180°C. Also shown in Fig. 5 is the geometrical relationship of the measurement viewing angle with

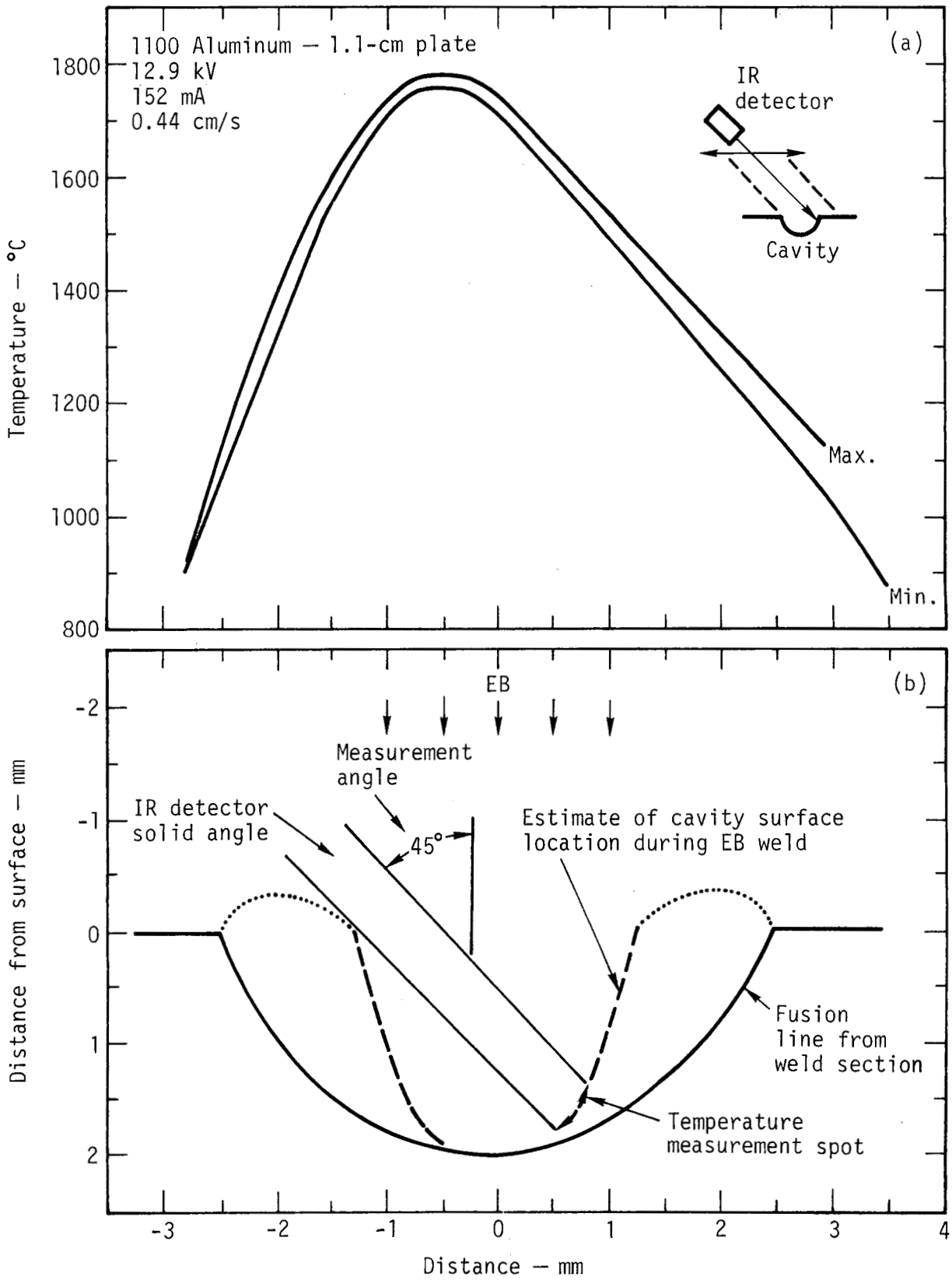

Fig. 5. (a) Temperatures measured across a weld cavity during one pass of the EB weld, and (b) diagram of the resulting weld section. The geometrical relationship between the infrared detector and the material surface is also shown.

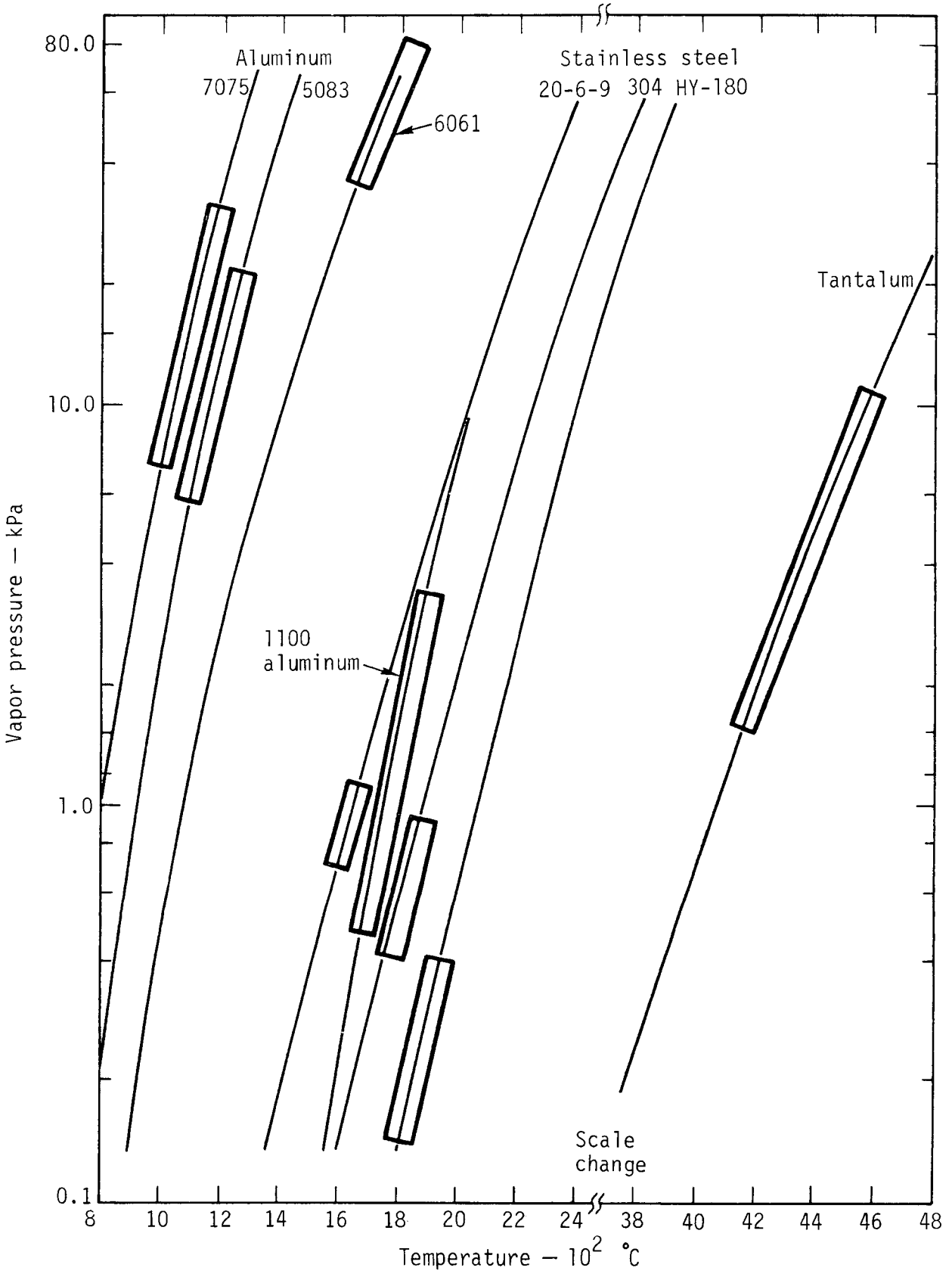

Fig. 6. Temperature-vapor pressure curves for materials welded. Bold face lines show the range of maximum temperatures measured during welding.

respect to the material surface. Because of the angle, temperatures are measured near the bottom of the cavity for shallow welds, and only at the cavity top for deep welds.

We are currently investigating the relationship between vapor pressure and temperatures for all of the materials welded in this study (see Fig. 6). The banded regions on the curves in Fig. 6 represent the range of maximum temperatures measured during welding. This allows qualitative conclusions to be made on the postulation that vapor pressure maintains the cavity shape during welding. If a minimum pressure is required, it should be large enough to overcome both the hydrostatic head of liquid metal that surrounds the cavity and the constricting force due to surface tension. For the materials welded (assuming 60% penetration and cavity radius = 0.4 mm), the calculated vapor pressures are 4.3, 9.6, and 11.3 kPa, respectively, for aluminum, steel and tantalum. The best agreement with pressures at measured temperatures are for the pure aluminum and tantalum. The steel and aluminum alloys show a little discrepancy. We calculated the vapor pressure data for the alloys using Dalton's Law and assuming that the percentage of elements is identical in both the vapor and solid state. If the more volatile elements evaporate at a faster rate during welding, then the vapor composition will be different than the solid composition. However, by chemically analyzing the vapor plated onto a glass slide during welding, we can better define the percentages of each element in the vapor state. Then the vapor pressure-temperature curves for alloys can be better defined.

Conclusions

Our major conclusions are:

- The temperature-measurement technique works and the system could be miniaturized. A miniaturized system could be inserted into any EB chamber with little or no disturbance to the existing chamber. Then we could take extensive measurements without disturbing the present welding procedure.
- Measured peak response is very sensitive to small changes in focus adjustment and could be useful for fine tuning the EB spot.
- The measured temperature does correlate with the required vapor pressure for relatively pure materials. The surface temperature of the cavity can be estimated within 100-200°C for pure materials not yet tested.
- The temperature increased slightly as the EB energy was increased.

What remains to be done is to determine whether temperature measurements can provide a means of indicating weld quality and establishing weld parameters.

QUALITY ASSURANCE FOR SYSTEMS AT THE LLL TRITIUM FACILITY

The Lawrence Livermore Laboratory operates a facility used for experimental work with radioactive gases and their compounds. The primary radioactive gas is tritium. A program was initiated by the Director's Office in 1971 to upgrade the tritium-handling systems in the building. It was thought that by using improved materials and fabrication techniques and by establishing a formal quality-assurance plan, the probability of tritium releases could be greatly decreased.

The upgrading program generally follows the guidelines set by the Atomic Energy Commission for nuclear plants. It establishes requirements and constraints for the design, fabrication, procurement, construction, and operation of safety-related structures, systems, and components in the tritium facility.

This article describes in general terms the procedures and techniques developed in implementing the quality-assurance plan. The upgrading program is still in progress, with several tritium-handling systems completed and others in various stages of development. Ten systems required modification.

The tritium-facility building is divided physically to provide two zones of differing relative hazard. The office area, where no work with dangerous or radioactive material is permitted, is approximately 560 m^2. The radioactive materials area, separated from the office area by an interlock, has an area of 1400 m^2. The ventilating system in the building is designed to keep air flowing toward the high-hazard areas as a means of avoiding contamination of the work environment. All building air exhausts through the laboratory hoods and the vault into two 30.5-m stacks. The flow rate through the stacks is 6.6 m^3/s and 12.3 m^3/s.

Fabrication of Systems

We describe below new techniques developed as part of the quality-assurance program.

Selection and Procurement of Materials. The primary material used in tritium-exposed systems is AISI Type 316 stainless steel, meeting LLL specification MEL71-001168A. It is a very stable austenitic steel, weldable, resistant to hydrogen embrittlement, and not subject to gross martensitic transformation when thermally cycled or plastically strained at cryogenic temperatures. It may be cold-worked to high strength levels (above 550 MPa yield) and still retain adequate ductility (greater than 25% elongation).

All 316 stainless steel components must be made of high-quality, specially processed, clean material so that stringers of oxides or sulfide-type inclusions cannot provide a leak path, regardless of how parts are oriented relative to the longitudinal or transverse mechanical working directions. This is controlled by strict specification requirements and quality control checks based on ASTM E-45, Plate III standards.

All high-pressure valves and fittings are made by Autoclave Engineering from 316 stainless steel meeting MEL71-001168A, Conditions B (80,000 minimum yield strength and 25% minimum elongation). The intermediate pressure components are manufactured from material meeting MEL71-001168A, Condition A. Cajon fittings and Nupro valve bodies fall within this category.

All primary tubing used in the tritium system must meet LLL specification MEL71-001150C or MEL681L. The former specification is preferred, but it is more difficult to obtain. In either case, we require 100% in-house ultrasonic inspection of all the tubing. We reject all tubing with a defect level greater than 0.05 mm deep and 0.76 mm long (any orientation, inside or outside surfaces). Surface finish, both inside and outside, is very important so that the ultrasonic signal-to-noise ratio will produce reliable oscillographic inspection records.

Using 316 stainless steel created several problems. First, high-quality nuclear-grade material with the cleanliness and chemistry we require must be purchased directly from the steel mills. This means it must be ordered in minimum lots of 2268 kg, with a minimum order of 227 kg for each size or shape within the order. Vendors of system components are reluctant to buy a mill quantity of steel to fill our small orders. What's more, it takes six months to a year to get the material from the mill.

To solve these problems we created a certified-material storeroom. This storeroom serves all tritium-handling systems and can therefore buy mill quantities of steel. Vendors draw on these supplies to make system components. The storeroom stocks components common to several systems (e.g., tubing, valves, fittings) as well as bars and billets from which specialty items can be made. As a result, lead time on component delivery can be reduced by as much as two years. About 75% of a tritium-handling system can be built from the materials in the certified-material storeroom.

For every item in the storeroom, we take the following steps:

(1) We examine the supplier documentation, such as certification of the chemistry and physical properties of the item.
(2) We inspect the item at the supplier.
(3) We perform extensive inspection and testing.

Manufacturing and assembly processes for component parts and systems must be specified because of their effect on the metallurgical properties of the material and on our design. In the beginning, many vendors were reluctant to change their processes to accommodate us. The small size of our orders, the complications of complying with our quality-assurance requirements, and the possible involvement of a subcontractor made filling our orders very unattractive. The certified-material storeroom has generally solved our supply problems. Because larger quantities can be ordered at a time, it is economically feasible for a vendor to change his processes and comply with our quality-assurance requirements. When the vendor will not provide the component we require, we then weigh the risk to the systems against the effort required to develop an in-house process. We sometimes use parts of a commercial assembly and incorporate items of our own design and manufacture. We can also pressure-test the equipment, and if necessary downgrade it. We took this approach with a commercial thermocouple vacuum gage tube needed to measure the pressure in vacuum systems.

Fabrication Standards. Strict application of the quality-assurance program to all systems containing tritium would be a near-impossible task. An absolute no-leak policy is clearly impossible and impractical. In normal maintenance operations on components exposed to tritium, small, unavoidable releases occur. Also, the expense involved in maintaining the highest quality standards on all equipment would be enormous. It became apparent that different fabrication guidelines had to be established, based on the release potential of particular systems or operations. The release potential of a system was defined in terms of the amount of tritium contained at a pressure in excess of one atmosphere. Three general types of construction were defined:

(1) Certified construction (fabrication, inspection, and testing according to a rigid set of procedures and specifications, following the quality-assurance program to the letter; all

steps are completely documented to verify compliance).

(2) Quality construction (some of the nondestructive testing and documentation is omitted).

(3) Standard construction (use of good, standard laboratory construction practices).

To help us define specific circumstances in which the more stringent construction techniques would be required, the Hazards Control Department at LLL provided an estimate of the maximum allowable routine-operation exposure from tritium release from the facility. Federal standards relating to accidental release allow a 500-mrem maximum annual dose for an individual. They also stipulate that the average annual dose due to accidental release for individuals in the surrounding population cannot exceed 170 mrem. We have taken a more conservative approach, accepting 500 mrem as the maximum allowable annual exposure for any person, but applying this standard, not to accidental release alone, but to our entire operation. Thus, under our standards, the average annual dose will be much less than 170 mrem.

Assuming a release consisting entirely of tritiated water, HTO (the worst and least likely case), we can calculate, on the basis of the above standard, a permissible release of 6700 Ci. This amounts to 0.67 g of tritium. T_2 would be from 400 to 1000 times less toxic than HTO. We thus set an upper release limit of 0.67 g of tritium for any apparatus or system that might plausibly convert tritium to HTO. A fully certified system would be required if the release potential were higher. For example, apparatus using heating elements or containing reactive metals and their tritides would be required to be fully certified or to incorporate secondary containment if more than 0.67 g of tritium were potentially releasable.

By adopting the concept of standard, quality, and certified construction, we can build safe equipment at much lower cost. The concept also allows us a crucial degree of flexibility in much of our research and development work. For example, some systems are designed to link fully certified sections to quality sections, provided that proper means of isolating the critical sections are incorporated.

Joint Design. We have taken the position that welded joints should be used in preference to mechanical joints whenever possible and practical. They are not as susceptible to leaks due to tampering or accidental loosening, and they do not have to be leak-checked before each run. On the other hand, they are initially more expensive (to make and to test), and they add to the difficulty of modifying or replacing components.

The basic welding procedure is specified in the ASME Boiler and Pressure Vessel Code, Section IX, 1971. Whenever possible, TIG fusion welds are followed by a second-pass TIG annual wire feed. The purpose of the latter procedure is to reduce the probability that microcracks in the two welds will line up. Specifications on the weld wire, weld wire qualification, weld joint design, and weld joint design qualification were developed at LLL.

Weld and testing procedures are clearly defined, and all welds are made by certified welders. A welder becomes certified by doing one practice weld and three test welds that are later radiographed, checked with fluorescent penetrant, and examined metallurgically to verify that the welding technique was correctly and consistently done. All joints are tested with liquid penetrant after a gas-pressure test to 150% of the maximum allowable working pressure. As many joints as possible are radiographed.

For high-pressure components, a high-pressure thick-walled tube is threaded into a mating component such as a valve or fitting, and then a seal weld is made. For low-pressure components, the socket weld is the basic joint.

In cases where weld joints are impossible or impractical, two types of mechanical joints are used, one for high-pressure components and one for low-pressure components. The joint for high-pressure components consists of a female part with a 60° cone, a threaded tube with a 59° cone end to fit into the 60° cone, a collar that threads onto the tube to provide an adjustable flange, and a gland nut that fits behind the collar. As the gland nut is screwed into the female housing, the assembly is seated. For low-pressure components, we use a metal-to-metal seal with a disposable metal gasket. The greatest drawback to this is that every time the joint is disassembled, the gasket must be replaced and the replacement gasket must be certified.

Secondary Containment. We cannot meet strict certified standards on all parts. In some cases, 316 stainless steel cannot be used; in others, no manufactured item meeting our specifications is available. For these situations, we use a component material sufficiently compatible with tritium to have a reasonable expected life (AISI 304 stainless steel, for example), and then we provide secondary containment. Any secondary-containment system must be able to contain the tritium until it can be removed. There must also be a way to monitor the secondary container for failure of the enclosed component and a way to remove tritium from the secondary container if failure occurs.

Our high-pressure gas system gives an example of secondary containment. The diaphragm compressor had too many parts and was influenced by too many uncertain manufacturing processes to be certified, so we modified some parts to make them more compatible with tritium and then enclosed the compressor in a secondary container.

In addition to secondary containment, we built into our systems mechanical devices designed to counteract operator error. Two examples are:

(1) Rupture disks. If, by accident, a wrong valve is opened and a high-pressure gas enters a low-pressure system, a rupture disk will burst, and the gas will flow to a containment system designed to contain the total gas volume.

(2) Series valves. For systems where rupture disks are not practical, two valves in series are used. Thus, only a double seat failure or double accidental valve openings will result in failure of the system.

Testing

Pressure Testing. Testing of the subassemblies in any given system is accomplished by pressurizing it with a 90% helium and 10% oxygen mix to 150% of the maximum allowable working pressure (MAWP) and then holding for 0.5 h. The pressure is then reduced to the MAWP and leak tested using a mass spectrometer capable of detecting a leak rate of 1×10^{-9} atmospheric cm^3/s. No detectable leakage is allowed.

We should perhaps explain why oxygen is used in the pressure-text mix. Tests have shown that 304 stainless steel will oxidize slightly and thus acquire a protective coating useful in preventing hydrogen embrittlement. Similar tests of 316 stainless steel have not been made, but we can reasonably assume that it oxidizes in the same way. It is theorized that oxygen in the pressure-test mixture described above will seep into microcracks that form during the 150% MAWP test, permitting oxidation. Since the system is never again pressurized to 150% MAWP, no new microcracks will occur, and the old ones are effectively protected by the oxide coating.

As a secondary check, the assembly is then tested at 140% MAWP for 2 h using deuterium. If a substandard part (made of nickel, for example) has inadvertently been used during assembly, it will be highly stressed under these conditions, and hydrogen embrittlement will cause failure. A safety note is written for each system describing other testing that is required.

When the system is operational, we require it to be pretested with deuterium to 140% of the anticipated experimental pressure prior to every use with tritium. No detectable leakage is allowable.

Documentation. The documentation required on the materials, fabrication, testing, inspection, assembly, etc. of a certified system is quite extensive. Since the engineering drawings provide the information required to purchase, fabricate, assemble, and test a system, we use the print as the index to this information.

Besides serving as an index, the "marked prints" are used as checkoff lists, signoff sheets, and "as-built" system drawings. When the assembly is complete, the print is checked and microfilmed to serve as an "as-built" permanent record of the assembly.

Concluding Remarks

Quality-assurance programs are both expensive and time-consuming. Presently, ours is a 17-person effort with a total cost of $700,000 per year. In addition to this, the certified-material storeroom employs three or four people in certification of materials and fabrication of standard subassemblies. The program took about two years to launch because of the time lag in obtaining high-quality materials from suppliers.

We have trained a number of people in system assembly. For obvious reasons, the emphasis here is on correctness and care, rather than on speed. In all phases of our work, well-trained people are a necessity, and their attitude towards quality assurance is crucial. Although we have established rigorous fabrication and testing standards, in the final analysis, the success of the program depends on how these people carry out their assignments.

FE

SLOSHING IN POOLS UNDER EARTHQUAKE-LIKE GROUND MOTION

Spent-fuel elements from nuclear reactors are stored in pool structures while waiting to be reprocessed. Pools now in use are about the size of a large swimming pool (~12 X 24 m) and from 9 to 14 m deep. Much larger pools, about the size of a football field, (~49 X 73 m) are being considered for future use. Because of this size, the pools may be divided into modules, again roughly the same size as the storage

pools now used. Modularization would enhance operational safety by isolating trouble spots and allowing localized clean-up. Earthquake-generated hydrodynamic pressures and water slosh-heights are important considerations in determining the effect of modularization. This article addresses the evaluation of these hydrodynamic responses to earthquake motion.

Although various techniques are available for evaluating hydrodynamic response, their validity for pools of the size used for storing spent fuels has not been firmly established due to a lack of experimental data on large pools. To obtain data, we performed experiments on large swimming pools near the Nevada Test Site during two underground nuclear events. The ground motions were very much like distant earthquakes.

Swimming Pool Experimental Setup

Two experiments were carried out: the first at the swimming pool (12.8 X 25.1 m) in Mercury, Nevada, during the Kasseri Event, October 28, 1975; the second at the Maslow Park swimming pool (12.8 X 22.9 m) in Las Vegas, Nevada, during the Muenster Event, January 3, 1976. The yield for both events was approximately the same.

The pool sites, relative to the event locations, are shown in Fig. 7. Mercury is roughly 80 km from the event site, Las Vegas about 160 km.

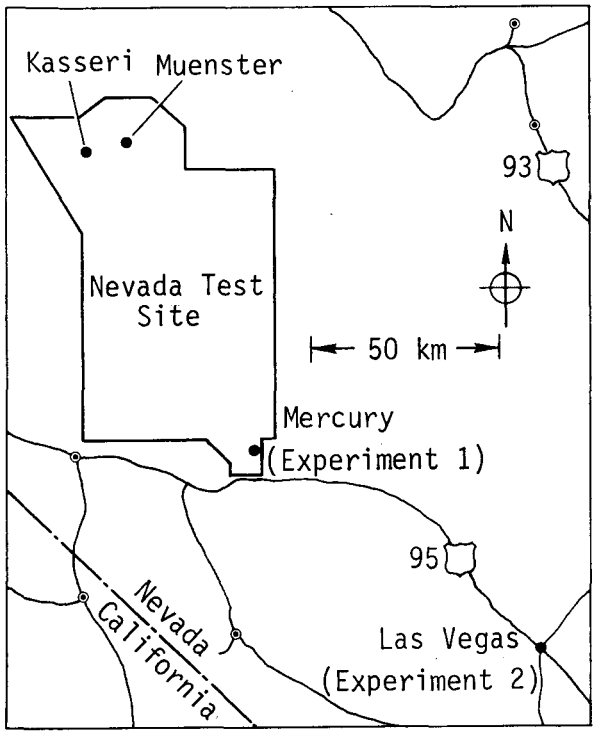

Fig. 7. Location of swimming pools relative to the Kasseri and Muenster underground nuclear events.

The ground acceleration-time history was monitored with Q-Flex Model No. QA-116-15 accelerometers, chosen for their ability to accurately capture low frequencies, and was recorded on magnetic tape. For the pool sizes investigated, the sloshing frequency was as low as 0.07 Hz. Ground motions in the longitudinal, lateral, and vertical directions were recorded at each accelerometer installation. The sloshing motion was recorded on motion picture film, 32 frames per second, at six locations for each pool. The slosh-height was indicated by aluminum targets painted with 2.54-cm gradations. Contact with the control center for the nuclear events was maintained by communication radio.

Hydrodynamic Theory and Analytical Techniques

Theories and methods available for evaluating hydrodynamic effects, including the classical theory, Housner's theory, finite difference methods, and finite element techniques, are discussed in Ref. 2. Some of these techniques are rather sophisticated and probably not necessary for the simple geometries (rectangular shapes with flat bottoms) expected for spent-fuel storage pools. The walls of such structures will be made of 1.2- to 2.1-m-thick reinforced concrete so that overall rigidity will be high. Housner formulated his theory[3] especially for rigid structures of simple geometry; his theory, therefore, is simpler than the classical one. Nevertheless, Housner[3] showed that the results given by his theory were within 2.5% of classical theory. Therefore, in terms of accuracy and ease of application, Housner's theory appears the most reasonable for the design of the pools, a view apparently shared by industry where the theory is widely used. Thus, we selected Housner's theory[3] for comparison with the experimental results.

Linear hydrodynamic response consists of two contributions: impulsive and convective. The impulsive pressure is the response to instantaneous acceleration. A portion of the water mass behaves as if it were a solid firmly attached to the pool. The mechanism, which appears straightforward, is affected only by possible nonlinearities. The convective response is associated with sloshing and results from low-frequency motions. This response is complicated by damping in the water as well as by possible nonlinearities and, consequently, is in greater need of experimental confirmation. Therefore, if Housner's theory is shown to be applicable with respect to its convective portion, thereby establishing that linearity holds, then the applicability of the impulsive portion could be assumed to follow. Consequently, our experiments focused on confirming the convective portion of the theory. For the pool size of interest, the frequency range for the first-sloshing mode is from

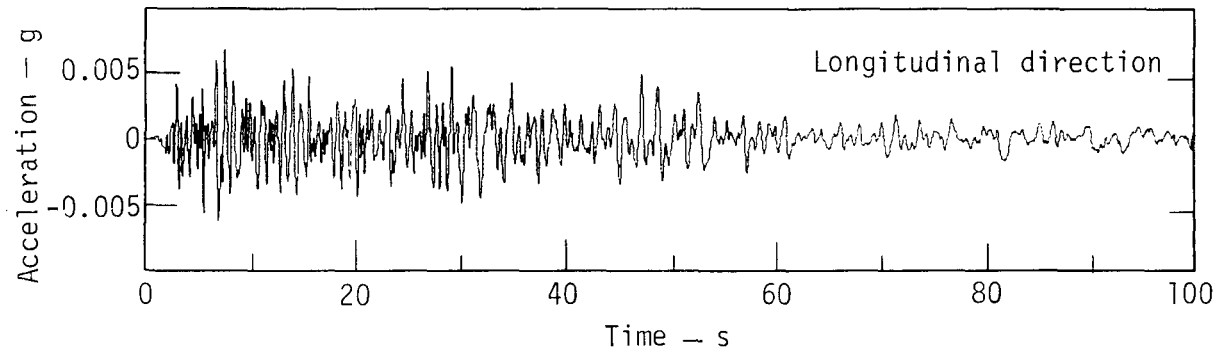

Fig. 8. Typical acceleration-time history. This example was recorded at the Maslow Park, Las Vegas pool.

0.07 to 0.25 Hz. Unfortunately, in the case of earthquakes, the response-spectrum values of these low frequencies often are not accurately determined.[2] Special care was taken in these experiments to assure that accurate values were obtained for the displacement-response spectrum at frequencies down to 0.07 Hz. Hydrodynamic pressures were not recorded because the expected values would have been too low for accurate determination at the magnitude of ground motion anticipated. The convective pressure is directly related to recorded slosh height, so that for our purposes the lack of pressure data was not critical.

The swimming pools used in our experiments were not flat-bottomed; the depth from one end to the other varied from about 1.1 to 3.4 m, with a mean depth of 2.0 m for the Las Vegas pool and 2.3 m for the Mercury pool. The pools were analytically treated as flat-bottomed with a depth equal to the mean depth. The flat-bottomed equivalence has been successfully applied to conical containers for evaluating the overall structural load and the slosh response up through the second slosh mode.[4,5] According to Ref. 4, for the equivalence to be valid, the container should not be extremely shallow, i.e., the mean depth to diameter ratio, h/D, should not be $\ll 0.25$. The effective h/D ratio for the swimming pools was 0.11 which is $\ll 0.25$. However, because the pools investigated are closer to being flat-bottomed than are the conical containers, we feel the flat-bottomed equivalence is valid. The depth of the pools varied gradually and only in one direction, never becoming zero as is the case along the entire circumference of a conical container. Good agreement between our data and theory lends support to the validity of this equivalence.

Experimental Results Compared with Theory

At the pool sites, the ground motion generated by the nuclear events was very similar to that of a distant earthquake. We recorded acceleration-time histories (Fig. 8) and then derived displacement-time histories. The resulting response spectra (Fig. 9) were comparable to those of an earthquake.

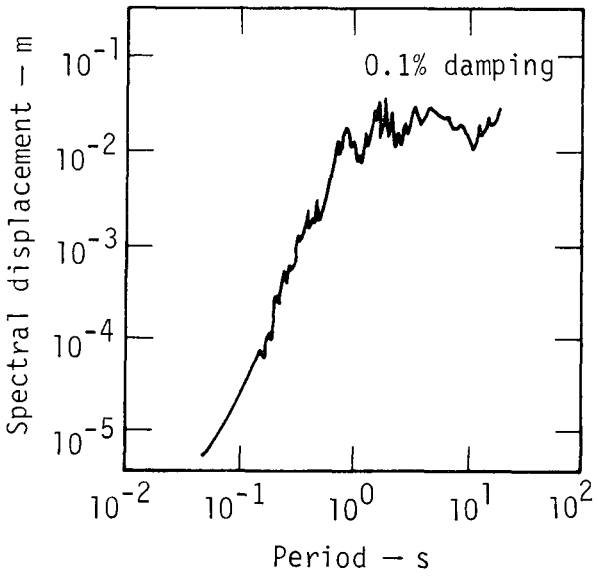

Fig. 9. Typical ground motion response spectrum. This example was recorded at the Maslow Park, Las Vegas pool.

Special care was taken to extract accurate values for the displacement-response spectrum from the acceleration records. To obtain spectral displacement, the effect of drift, inherent in all such instrumentation systems, must be accounted for in the manipulations. A refinement of Trifunac's procedure, as explained by Jackson, was followed in making the necessary drift corrections. However, in our case, an additional improvement was available, because 1/2 min of quiescent data were taken before the ground waves from the nuclear event arrived. This provided information on drift alone.

The water response data recorded on motion picture film revealed high-frequency, small water waves generated by the first arrival of ground motion. These died down rather quickly, and the first sloshing-mode then dominated. The maximum amplitude of sloshing occurred about 60 s after arrival time. The total motion can be considered as a summation of the longitudinal and lateral slosh motions with the slosh frequencies differing in the two directions. At a given location in the pool, the most probable maximum slosh amplitude is the root mean square sum of the contributions from the two directions. A representative slosh amplitude was extracted from each data record by randomly selecting several large excursions between a minimum and a maximum and averaging the readings.

Theoretical slosh heights at each data-recording station were evaluated using Housner's theory.[3] Only the first sloshing-mode was considered. Spectral displacements used in the slosh amplitude determinations were those at the center of gravity of the total water mass. These values at the center of gravity were calculated from values determined at the opposing corners of the pool using a linear variation of motion across the pool.

Damping in the water depends on pool geometry and size. Expressions for circular vessels were represented in Refs. 5 and 6. Applying expressions for circular vessels[2] to the swimming pools and using an equivalent circular geometry indicates the damping in the water should be nearly zero. The displacement response spectra for a typical earthquake are practically the same for all values of damping equal to and below 0.1% of critical. Therefore, a damping value of 0.1% was used for evaluating theoretical slosh amplitudes (see Table 2). The slosh amplitude was estimated to differ by only 2.5% between 0.1 and 0% damping.

The average of ratios of the theoretical to the experimental slosh amplitude value (T/E ratio) is 0.95 for the Mercury experiment and 0.93 for the Las Vegas experiment. (Table 2). The fact that the pools were not really flat-bottomed would partially account for the individual station discrepancies. The average value of the ratio is a good indication of the overall agreement, which is more significant than station by station agreement, and the comparison with theory is excellent on this basis.

Applicability to Spent-Fuel Storage Pools

This experimental study covered hydrodynamic characteristics of pools in the size range of interest for spent-fuel storage. The first sloshing-mode frequencies of the swimming pools were comparable to those projected for spent-fuel storage pools. Damping in the water decreases with increasing pool size. Therefore, nearly zero damping found in the swimming pools would hold also for larger spent-fuel storage pools.

We addressed the validity of applying a linear theory such as Housner's[3] to spent-fuel storage pools subjected to actual earthquakes by evaluating the sloshing response to the response spectrum specified in Regulatory Guide 1.60.[2] A maximum ground acceleration of 0.2 g was taken as representative of earthquakes east of the Continental Divide. We compared the slosh amplitudes evaluated for the pool sizes of concern with the linear range as prescribed by a criterion suggested by Kana and Dodge.[6] The criterion specifies that linearity applies if the slosh amplitude is no greater than one-tenth of the pool length in the direction of concern. The calculated slosh amplitudes for the pool sizes are within the linear range except for two cases which are slightly beyond the linear range. Nonlinearity tends to give the same effect as increased damping in that the slosh height will be

Table 2. Experimental vs theoretical water slosh amplitudes

	Mercury Experiment			Las Vegas Experiment		
Target station	Housner's theory (cm)	Test data (cm)	T/E ratio[a]	Housner's theory (cm)	Test data (cm)	T/E ratio[a]
2	0.58	0.66	0.88	1.24	1.24	1.00
3	0.81	0.66	1.23	1.55	1.52	1.02
4	0.74	0.86	0.85	1.30	1.42	0.91
5	0.71	0.74	0.96	1.27	1.52	0.83
6	0.81	1.04	0.78	1.52	1.78	0.86
7	0.58	0.58	1.00	1.24	1.32	0.94
Average T/E ratio[a]:			0.95			0.93

[a]Theoretical/experimental ratio.

less than predicted by linear theory. Therefore, in terms of the slosh height, and thus the convective hydrodynamic pressure as well, the results obtained from the linear theory will be conservative for the two cases lying slightly beyond the linear range of response.

Summary and Conclusions

The results of this study indicate that Housner's theory[3] is adequate for evaluating hydrodynamic effect in spent-fuel storage pools subjected to seismic loading. The damping in the water for the pool sizes of concern is very low. A critical damping value of 0.1% was found to be sufficiently small for the pool sizes examined. The response spectrum remains virtually unchanged for lower damping values. The displacement-response spectrum at frequencies in the range of 0.07 to 0.25 Hz governs the convective response. Unfortunately, values reported at these frequencies are not always accurate.

AES

CALCULATIONS OF TWO-PHASE DISPERSED DROPLET-IN-VAPOR FLOWS INCLUDING NORMAL SHOCK WAVES

A two-phase turbine has been proposed as a geothermal energy conversion device. Motive fluid for the turbine will be a very low quality (vapor mass fraction), two-phase steam-water mixture with impurities. This study was initiated in response to the need for an analytical technique for predicting the flow through the nozzle and blade passages of such a device.

Considerable attention has been focused on high-quality two-phase flow phenomena for condensing steam turbine applications.[7] Satisfactory prediction of high-quality flow does not require the sophistication necessary for that of low-quality flow. In particular, complete coupling between the two fluid phases is not required for a reasonable approximation in high-quality calculations because momentum transfer between phases is not a significant factor. Thus, for high-quality flow, analytical design procedures based upon single-phase turbine flow models have been sufficient.

By contrast, when a two-phase mixture containing characteristically 65% liquid by weight but less than 0.1% liquid by volume (as is expected with geothermal energy extraction) is used for the working fluid, conventional design techniques no longer correctly model the physics of the problem. For example, the choking velocity in a two-phase mixture is lower than in either phase alone and its value is dependent upon several factors including the local ratio of quantities of liquid to vapor.

Because of the complexity of the phenomena involved, two-phase flow calculations can best be treated numerically. Several approaches have been developed, but they were not considered suitable for the geothermal application. Thus, we developed a new approach, based on some unique concepts.

Before commitment to a two-dimensional model, we implemented a one-dimensional model to verify the new approach. Because the one-dimensional formulation includes area change, it is referred to as "quasi-one-dimensional." The assumptions used in developing our model include:

(1) Design considerations, such as geothermal well-head fluid state points and the desire to extract maximum energy per unit of flow, require that the fluid velocities in the turbine be supersonic relative both to the two-phase choking velocity and to the vapor-sound velocity. Such high velocity, combined with the very low liquid volume fractions involved, permit consideration of the two-phase mixture as droplets in a vapor continuum.

(2) The flow field through a turbine is transient in time by definition; however, conventional turbine design techniques usually consider only steady-state solutions. A steady-state solution is desirable, both because experience indicates its sufficiency and, because it significantly reduces the complexity of the calculation.

(3) Our model is inviscid except for drag between the vapor and the droplets. This assumption allows calculation of the general flow while boundary layer corrections can be made with a two-phase boundary layer model that has been developed by Crowe.[7] The inviscid vapor assumption is based on inertial forces of the droplets being substantially greater than other droplet forces resulting from viscous vapor interaction.

(4) Droplets are assumed to remain spherical. Evaporation or condensation is assumed to occur uniformly over the surface of the droplets.

(5) Thermodynamic equilibrium is assumed to exist between liquid and vapor. Based on thermal relaxation times,[8] which are small for droplets of the size range of interest (<20 μm), thermodynamic equilibrium appears theoretically justifiable. Experiments, which will be discussed later, further justify this view. For the equilibrium case, interphase

momentum coupling is required in the form of droplet drag.

There are two additional levels of sophistication beyond the equilibrium assumption accounting for nonequilibrium phenomena:

(1) The macro nonequilibrium view assumes that pressure, but not temperature, equilibrium exists between phases. Thus, instead of remaining on the saturation lines, as in the thermodynamic equilibrium case, the liquid state point may pass into the compressed liquid region and the vapor state point may pass into the superheated vapor region. For very small droplets ($<<1$ μm diameter), the droplet liquid pressure should be corrected for surface tension. Momentum and energy coupling terms must be used to model the interphase drag and heat transfer.

(2) The macro nonequilibrium view assumes both pressure and temperature are not in equilibrium between phases. Here, the details of the pressure gradients around each droplet; local thermal, mass, and momentum boundary layers; and droplet shape must be addressed. The micro nonequilibrium view does not lend itself to continuum modeling.

Since deviation from equilibrium appears to be minor, the additional complexity introduced by nonequilibrium models is not justified at this time. Were detailed shock structure of immediate interest, the nonequilibrium effects would appear to be necessary.

The turbine flow will be supersonic both in the nozzle and relative to the turbine blades. To effectively calculate blade performance, oblique shocks occurring at the leading edge must be included. The blade passage itself requires at least a two-dimensional description. Parallel flow should issue from the nozzle exit. This requires two-dimensional calculation capability since standard two-dimensional nozzle design techniques do not apply to two-phase flow. Off-design performance is an additional consideration both for the blades and nozzles. Here, both normal and oblique shocks can occur.

Selection of Governing Equations

With the above assumptions and simplifications, we chose a suitable set of equations. For one-dimensional flow, two continuity equations, two momentum equations, two energy equations, and equation-of-state relations for the saturation properties of the liquid and the vapor are necessary. The continuity, momentum, and energy equations may be formulated in a Lagrangian or Eulerian reference frame, or the formulations may be mixed for convenience. We chose to introduce equations for the two-phase mixture of vapor and droplets in Eulerian form and equations for individual droplets in Lagrangian form. Explicit interphase source terms are thus eliminated.

Governing Equations and Solution Procedure

The two-phase mixture equations of continuity, momentum, and energy, derived in the Eulerian reference frame, written in vectorized conservative form are given by:

$$\frac{\partial \bar{U}}{\partial t} + \frac{\partial \bar{E}}{\partial Z} + \bar{H} = 0, \qquad (1)$$

where:

$$\bar{U} = \begin{bmatrix} \rho A \\ \rho A[U_v X + U_d X + U_d(1 - X)] \\ \rho A\left[X\left(\frac{U_v^2}{2} + e_v\right) + (1 - X)\left(\frac{U_d^2}{2} + e_d\right)\right] \end{bmatrix}$$

$$\bar{E} = \begin{bmatrix} \rho A[U_v X + U_d(1 - X)] \\ \rho A\left[U_v^2 X + U_d^2(1 - X)\right] + pA \\ \rho A\left[U_v X\left(\frac{U_v^2}{2} + h_v\right) + (1 - X)U_d\left(\frac{U_d^2}{2} + e_d\right)\right] \end{bmatrix}$$

$$\bar{H} = \begin{bmatrix} 0 \\ -p\frac{dA}{dZ} \\ 0 \end{bmatrix}.$$

Table 3 defines the terms for all equations used in this article. The equations are introduced in the above form to facilitate their solution using the time-dependent MacCormack technique.[9] This is a noncentered differencing scheme requiring no explicit artificial viscosity. By using time dependence, hyperbolic equations are obtained for both the subsonic and supersonic flow regimes.

The momentum equation for an individual droplet, derived in the Lagrangian reference frame, is given by:

$$\rho_d U_d \frac{dU_d}{dZ} = \frac{3\rho}{4} v \frac{C}{D}(U_v - U_d)|U_v - U_d| - \frac{dp}{dz}. \qquad (2)$$

Table 3. Definition of symbols used in equations

A = Area (A* refers to nozzle throat)
C = Droplet Drag Coefficient
D = Droplet Diameter
e = Specific Internal Energy
$\overline{E}$ = E Vector
h = Specific Enthalpy
$\overline{H}$ = H Vector
$\dot{m}$ = Mass Flow Rate
p = Pressure
R = Mass Flow Rate Ratio
t = Time
U = Velocity
$\overline{U}$ = U Vector
X = Mass of Vapor/Unit Mass of Mixture
Z = Distance
μ = Viscosity
σ = Surface Tension
ρ = Density (mixture density unsubscripted)

Subscripts

v = Vapor Phase
d = Droplet Phase
e = Exit
o = Inlet
s = Isentropic
t = Total

This equation represents the trajectory of a single droplet for given initial conditions. Because the solution sought is for steady state, the initial conditions for all droplets of a given size, beginning at a particular point in space, may be assumed to be the same. Furthermore, the trajectory of a single droplet is the locus of all droplets of the same initial conditions, throughout problem space.

Because the equilibrium model was used (though the technique could be modified to consider the macro nonequilibrium case), one can eliminate either the continuity or the energy equation related to the droplet field. The use of a continuity relation is simplest and is given by:

$$\frac{D}{D_o} = \left[\left(\frac{1-X}{1-X_o}\right)\left(\frac{\rho}{\rho_o}\right)\left(\frac{\rho}{\rho_d}\,do\right)\left(\frac{U}{U_{do}}\,d\right)\left(\frac{A}{A_o}\right)\right]^{1/3}. \quad (3)$$

Equation-of-state relations (saturation properties as a function of pressure) are introduced in two groups: the first to be used with the mixture equations, the second to be used with the droplet equations. These two sets of relations are given by:

$$\rho_v = \rho_v(p),\ \rho_d = \rho_d(p),\ h_v = h_v(p),\ e_d = e_d(p) \quad (4)$$

and

$$\mu_v = \mu_v(p),\ \sigma = \sigma(p). \quad (5)$$

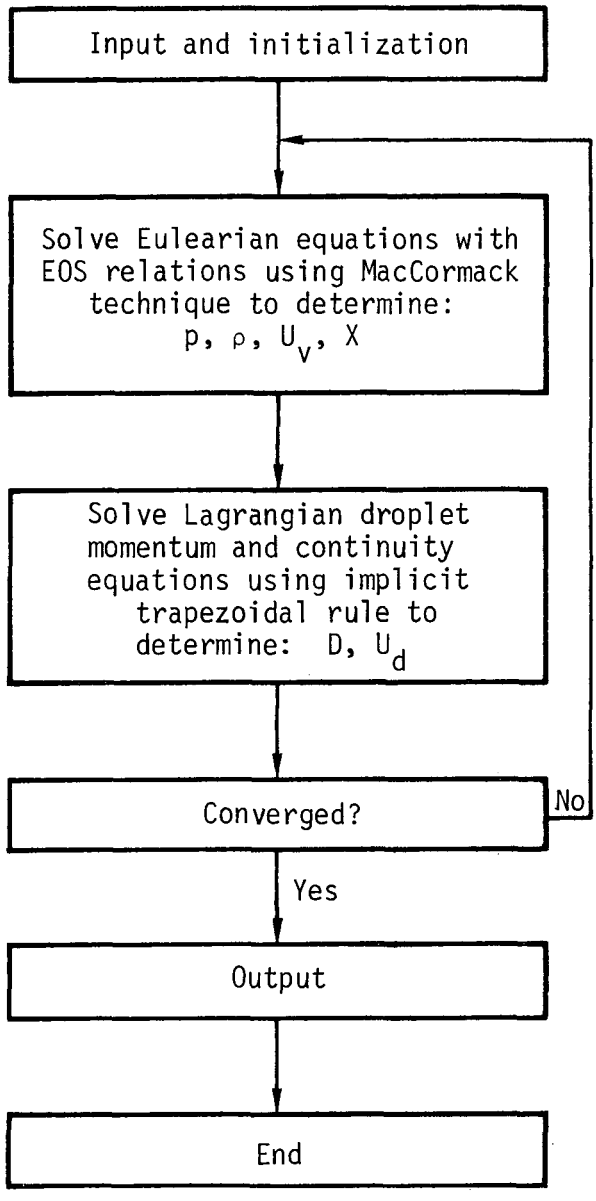

Fig. 10. Numerical solution scheme.

Figure 10 gives the numerical solution scheme. A calculational grid is selected for a given duct geometry and initial estimates of pressure, vapor velocity, droplet

velocity, and local mass fraction are provided. An iterative procedure, which alternates between the Eulerian and the Lagrangian systems of equations, is used to determine the final steady-state solution. The Eulerian equations [Eq. (1)] are solved with the saturation properties [Eq. (4)] of the liquid and vapor using the MacCormack differencing scheme. The result of this portion of the calculation is to determine new iteration values of pressure, mixture density, vapor velocity, and mass fraction for each calculational cell. Using this information the Lagrangian droplet momentum equation [Eq. (2)], the droplet continuity relationship [Eq. (3)], and additional saturation properties [Eq. (5)] are solved to determine the new iteration values of droplet diameter and velocity. For this portion of the procedure, integration of the momentum equation is accomplished using an implicit form of the trapezoidal rule, determining the new iteration values of droplet velocity and diameter. The procedure is then repeated, beginning again with the solution of the mixture equations, until convergence is reached.

A significant calculational simplification is accomplished, when steady-state solutions are desired, by using the Lagrangian form of the droplet momentum equation [Eq. (2)]. This equation, representing a single droplet, is solved as though steady state has been achieved before problem convergence is reached. In one dimension, only one trajectory need be considered, while in two dimensions, more trajectories must be used (however, only enough to allow interpolation of droplet behavior throughout the flow field.)

The solution procedure was originally designed to include varying the relative frequency of Eulerian and Lagrangian iterations. Having experimented with this option, we found that one for one was the best relative frequency – both for problem stability and for calculational speed.

The MacCormack algorithm operates in conservative variables, returning to the primitive variables twice during the two-step differencing scheme. The conversion from conservative to primitive variables, requiring a root finder for non-perfect gases as in the case of water vapor, can be calculationally expensive. The full A.S.M.E. equation of state for water was employed, until it was found that over 80% of the running time was equation-of-state related. This was remedied by forming cubic spline fits for the saturation properties of interest [Eq. (4) and (5)]. With this modification, running times for 100 spacial step problems are typically between 1/2 and 5 min on a CDC 7600, depending on the adequacy of the initially specified conditions and whether or not normal shocks occur.

If the macro nonequilibrium model is used, the Lagrangian droplet energy equation and an interphase energy-heat transfer term must be added. The latter is subject to uncertainty. In addition, the equation of state would be a function of two variables rather than only one. A very fast equation-of-state routine would be required to efficiently handle real fluid effects. These additional equations coupled with the more complex equation-of-state formulation would lead to a considerable increase in problem solution time.

Boundary Conditions

The calculational technique must employ properly specified boundary conditions. Four possible boundary conditions must be considered: both subsonic and supersonic duct entrance and exit flow conditions. The duct is specified to have a constant area for the first and last spacial steps in all cases.

(1) For subsonic entrance conditions, all primitive variables are invariant with time except velocity. The vapor velocity and droplet velocity remain unspecified but retain a constant ratio (slip). The spacial gradient of all variables is specified zero at the entrance. In terms of the conservative variables, the time derivative of the U vector and the spacial derivative of the E vector are set to zero.

(2) Supersonic entrance conditions require that all gradients are zero and all variables are invariant in time. Thus the time and space gradients of the primitive and/or the conservative variables are zero.

(3) For supersonic flow at the exit, all variables are unspecified. The spacial gradients of all primitive variables (and/or the E vector) are set to zero.

(4) Subsonic flow at the exit requires that the vapor velocity[10] (rather than the pressure) is defined at the exit while all other variables remain unspecified. The spacial gradients of all primitive variables (and/or the E vector) are set to zero. Assuming that the Rankine-Hugoniot relations can be satisfied by the defined vapor velocity, this boundary condition causes a normal shock to occur when initially supersonic flow is present in the duct.

We found that calculating the spacial gradient of the area for the two-step MacCormack algorithm required special treatment. The area gradient term appearing in the H vector must be evaluated using the local spacial gradient of the area consistent with the forward or backward differencing step.

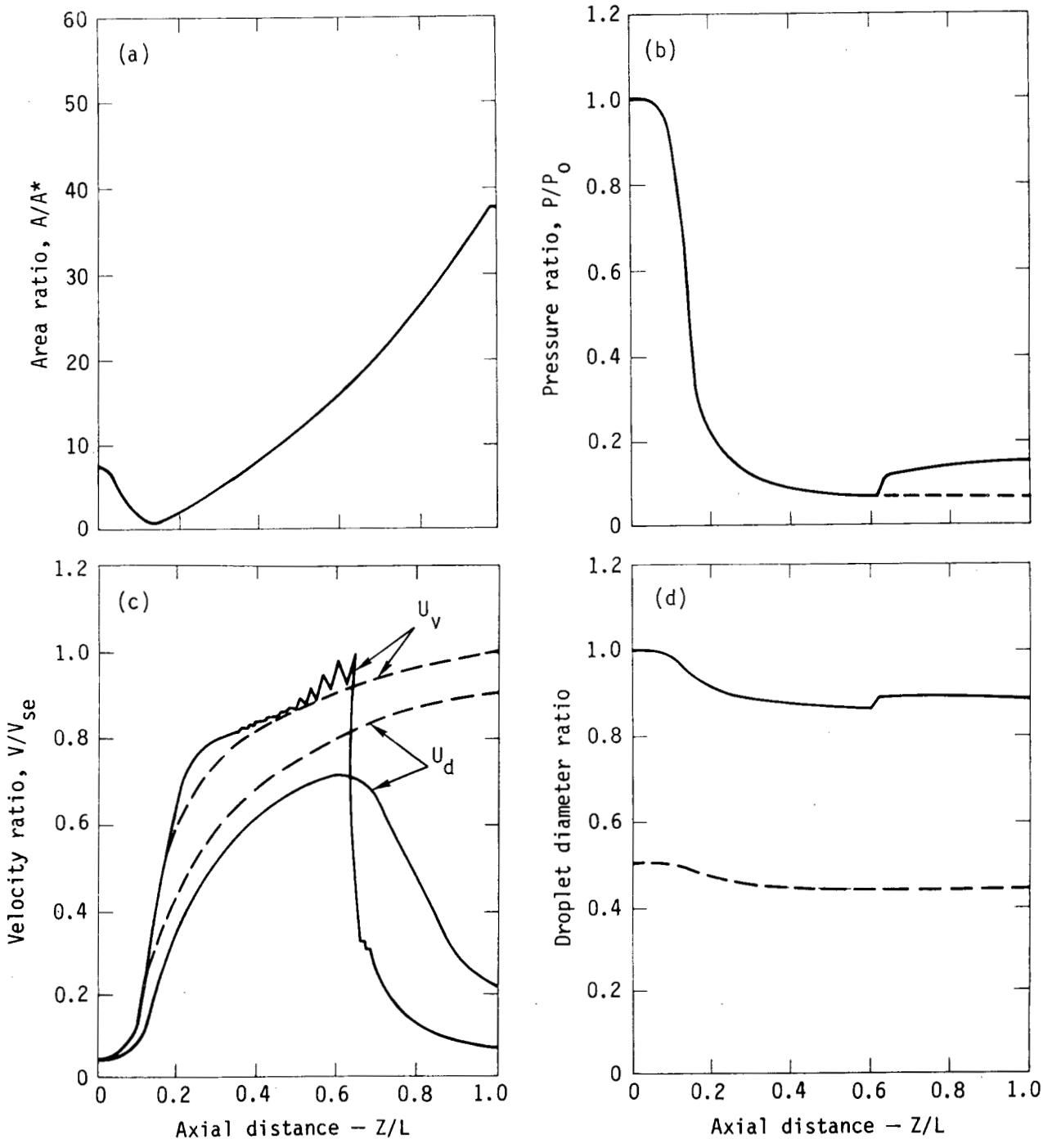

Fig. 11. (a) Nozzle area profile for one-dimensional calculation. A^* equals 6.38×10^{-5} m^2 and L equals 0.11 m. (b,c,d) One-dimensional calculational results for an optimum expansion through the low-quality nozzle (dashed lines) and for the low-quality nozzle including a shock wave (solid lines). Parameters were: P_o, 2.41 MPa; X_o, 0.155; L, 0.11 m; U_{ve}, 61 m/s; U_{se}, 700 m/s; D_o, 10 μm (droplet evaporation only). The various graphs show (b) pressure, (c) velocity, and (d) droplet diameter as a function of distance along the nozzle.

Example Calculations and Comparisons with Experimental Measurements

In this section, one-dimensional calculational results are presented for pressure ratio, velocity ratio, droplet diameter ratio, and mass-flow-rate ratio as a function of distance along two representative nozzles. For this experiment we designed a low-quality two-phase steam-water flow. Its area ratio profile is shown in Fig. 11a. Calculated optimum expansions as well as

those involving normal shocks are included for the low-quality nozzle. Experimentally determined pressure profiles are then compared with predicted pressure profiles determined using the calculational technique.

Predicted optimum expansions in the low-quality nozzle are shown in Fig. 11b-d. The droplets were allowed to evaporate, but not to break up.

Figure 11b-d also shows results of the low-quality nozzle, but with a normal shock included. The oscillations in the region of the shock are typical of the MacCormack technique with no explicit artificial viscosity specified and present no difficulty with respect to interpretation. Pure vapor shocks occur within one to three spacial steps with the MacCormack algorithm,[11] providing excellent spacial resolution. It is of interest to note that the shock width is considerably greater in the two-phase case than for pure vapor. In pure vapor, of course, calculations across a shock do not indicate shock structure but instead locate the shock and provide correct fluid conditions on either side of the discontinuity. Physically, the additional shock width is easily explained by the presence of the droplet phase. The liquid droplets have high inertia and are coupled to the vapor through droplet drag, which is dependent on the relative velocity between phases. The droplets tend to pass through the vapor discontinuity and than experience deceleration after the fact. As a result of this interaction, the vapor phase discontinuity becomes more gradual. Zoning in the calculations presented was not necessarily intended to be fine enough to model two-phase shock structure. In addition, the appropriateness of the equilibrium assumption could be questioned if the purpose of the calculation was detailed shock structure. Nevertheless, these calculations do show significant enough deviation in behavior from calculationally determined pure vapor shocks that indications of shock structure do appear to be evident and consistent with physical reasoning.

To test the applicability of the calculational procedure we measured the pressure distribution in the low-quality nozzle. Testing was performed in the two-phase flow test facility described in Ref. 12. Static pressure taps were installed at 26 approximately equally spaced axial locations spiraling between the entrance and the exit. Pressures were measured with strain-gage-type pressure transducers.

The pressure profile comparisons between calculations and experiments are presented in the traditional nozzle format: pressure ratio versus area ratio. Figure 12 shows this comparison for an ideal expansion in a low-quality nozzle. The agreement is within the experiment accuracy. An investigation of droplet diameters and velocities is presently in progress. Inferential droplet diameter estimates based on nozzle thrust[13] and on trajectory curvature in turbine blade passages indicate that the droplet sizes used in these calculations are well within the range encountered in the experiments. The excellent agreement of calculated and experimental results supports the validity of the equilibrium assumption.

To investigate flow through the low-quality nozzle for off-design exhaust conditions, a ball valve was mounted at the exit of a transition duct which was attached to the nozzle. Figure 12 also compares the measured and calculated pressure distribution for off-design nozzle back pressure. The experimental curve deviates from the quasi-one-dimensional prediction. For the same exit pressure, the predicted results exhibit a much more defined shock than experimental results would indicate. We think this is

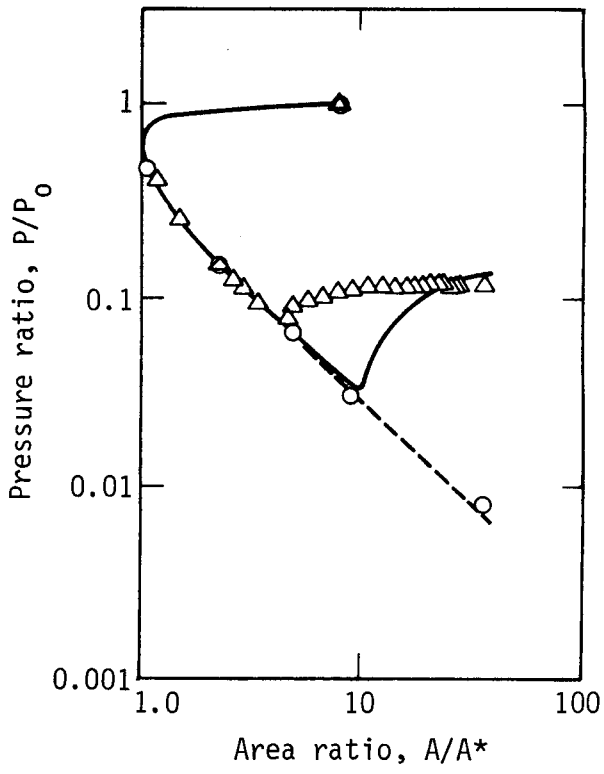

Fig. 12. Comparison of predicted and experimental pressure profiles for an optimum expansion through the low-quality nozzle (dashed line) and through the low-quality nozzle including a normal shock wave (solid line). Parameters for the optimum expansion (data indicated by ○) experimental results were: P_o, 2.59 MPa; and X_o, 0.15. Parameters for the expansion with a normal shock wave (data indicated by △) experimental results included: P_o, 2.47 MPa, and X_o, 0.153. Predicted result parameters were: P_o, 2.41 MPa, and X_o, 0.155. A* was 6.38×10^{-5} m^2 for all cases.

due to the occurrence of an oblique shock and boundary layer separation. We see this type of two-dimensional flow field rather than the predicted normal shock because the large divergence angle of the nozzle invalidates the one-dimensional flow assumption when separation is present. Similar separation phenomena and resultant pressure profiles are observed[14] in nozzles with considerably smaller divergence angles than the low-quality two-phase nozzle. The comparison indicates the importance of accounting for two-dimensional flow.

AES

Conclusions

The assumption of equilibrium between phases for two-phase nozzle flow without shocks is supported by comparisons of calculated and experimentally determined pressure profiles. Comparisons of predicted and experimental flows with shocks and the requirements for calculation of blade and nozzle flow support the need for a two-dimensional model. The stability and performance of the quasi-one-dimensional model presented justifies extension of the technique for the two-dimensional flow analysis as intended.

RADIATION DAMAGE STUDIES AT THE ROTATING TARGET NEUTRON SOURCE FACILITY

D-T fusion reactors will subject materials to damage from high-energy neutrons. To study the response of materials to this exposure, experiments are being performed at LLL's Rotating Target Neutron Source (RTNS-I) facility by every major materials laboratory in the U.S. To interpret the experiments, it is necessary to be able to calculate the energy spectrum of atoms recoiling from neutron interactions and other radiation damage parameters such as rates of production of displaced atoms and gaseous impurities. We have developed a computer code and performed these calculations for many materials exposed to the RTNS-I neutron spectrum. This code can be used to calculate radiation damage parameters for any neutron spectrum.

The RTNS-I facility consists of a high-intensity deuteron beam and a rotating, water-cooled target (see Fig. 13). The insulated core transformer (ICT) accelerator used in RTNS-I presently delivers a 15-to 25-mA deuteron beam collimated to a diameter of

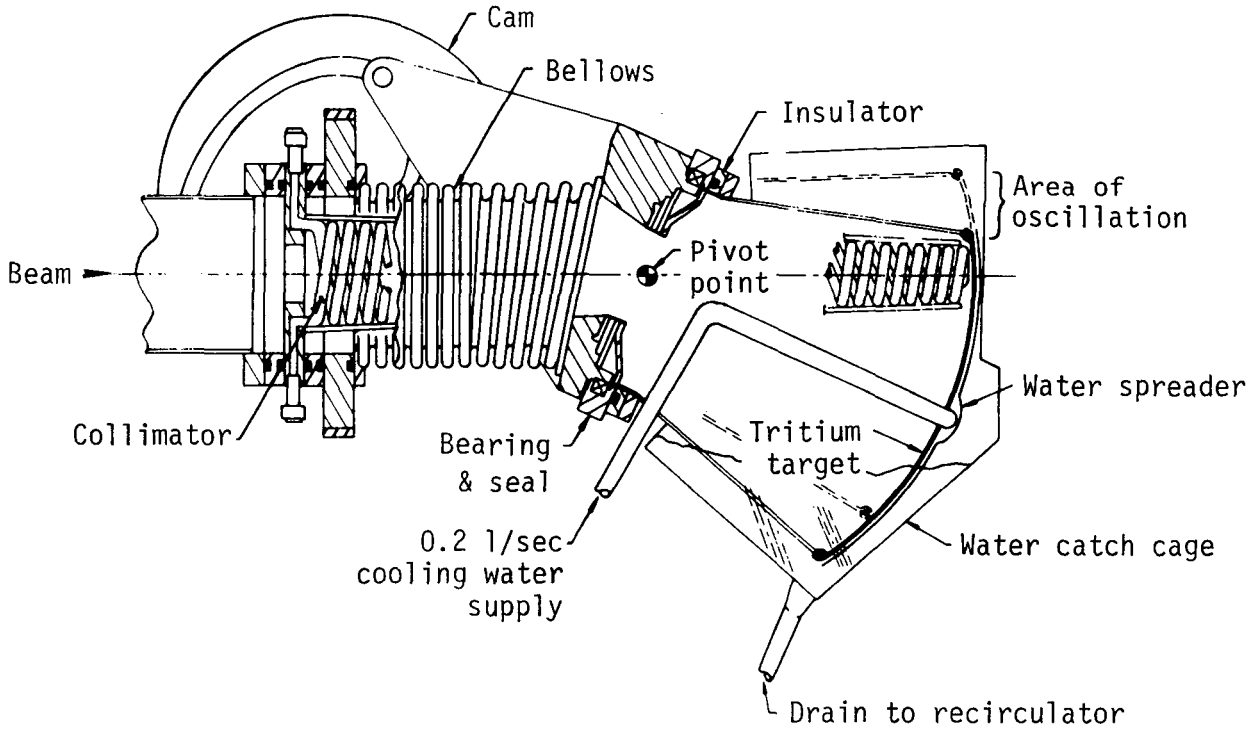

Fig. 13. Target system of RTNS-I.

Table 4. Lawrence Livermore Laboratory – 14-MeV neutron sources

	RTNS-I	RTNS-II	
	Present operation	Initial operation	Upgraded operation
Supply, mA, kV	60,400	300,500	600,500
Target current, mA	20	40 to 160	400
Beam diameter, cm	0.6	0.6 to 1.0	1.0
Power density, kW/cm^2	30	60 to 80	200
Target diameter, cm	23	46 to 70	70
Rotation speed, rpm	1100	5000 to 10 000	10 000
Source strength, n/s	5×10^{12}	1 to 4×10^{13}	1×10^{14}
Small sample flux, n/cm^2 s	2×10^{12}	4×10^{12} to 1.6×10^{13}	?
Target lifetime, h (20% yield drop)	100	100	?
Operational	Presently	1 July 1978	?

1.6 cm. Most of the current is concentrated to within less than half of this diameter. Fifteen-MeV neutrons are produced by deuteron bombardment of the tritium absorbed in the titanium target. The target is rotated at high speeds and is water-cooled to dissipate the large amount of power in the deuteron beam. Table 4 summarizes the main parameters of RTNS-I and also of RTNS-II, which will become operational in 1978.

Damage Energy Calculation

The computer program input requires material cross-section and angular distribution data for a particular material along with the incident neutron spectrum of interest. The energy-dependent cross-section and elastic distribution data are taken from the Livermore Evaluation Nuclear Cross-Section Library. These data are also used for LLL neutron transport calculations. The neutron flux and group boundary structure is defined by the user. Isotopic data and the threshold energy for displacement in the primary event are also required as input data. Linear interpolation is used in matching input flux, cross sections, and energy values and also in subsequent calculations.

The calculational procedure basically utilizes the input data combined with classical and relativistic mechanics to obtain the primary recoil energy and damage-energy spectra for the material of interest. The main nuclear reactions considered are elastic, (n, n'), (n, 2n), and (n, +). For RTNS, the (n, γ) reaction is not important in damage production and is not included. For elastic reactions, we use input angular distributions, and for nonelastic reactions we assume isotropic scattering. For nonelastic reactions in which the secondary particles consist of one or more neutrons, the energy distribution of the secondary particles is chosen from a nuclear temperature plus a pre-equilibrium component. Only the first particle out is considered. For outgoing charged-particles, we assume that the energy spectrum is Gaussian-centered at the Coulomb energy, dropping to 1% of the maximum value for zero-emitted energy.

The principal steps in the calculations are:

(1) The input spectrum is plotted.
(2) The input flux is partitioned, and average energies and cross sections are calculated for each group. All neutrons within a group are now assumed to be of the calculated average energy and cross section.
(3) A matrix containing flux-weighted cross sections for each reaction type and each neutron energy group is calculated.
(4) The normalized "primary knock-on atom" (PKA) spectrum for elastic recoils is calculated for each group.
(5) The nuclear temperature is interpolated from tabular values.
(6) The normalized PKA spectrum resulting from inelastic collisions is calculated and plotted for each group.
(7) The normalized PKA spectrum for charged-particle recoils is calculated and plotted for each group.
(8) All spectra are collapsed into a single primary-recoil spectrum. Plots are made of the resulting primary-recoil spectrum as well as the normalized integral of the spectrum (fraction of recoils with energy greater than the minimum for displacement).
(9) The primary recoil spectrum is now converted to a damage-energy spectrum by using

theoretical expressions derived for damage efficiency of creating atom displacements in materials. Plots are made of the damage-energy spectrum as well as the normalized integral of the spectrum (fraction of displacement in cascades with energy greater than minimum).

The integral of the damage-energy spectrum is a measure of the damage effectiveness of the input neutron spectrum. This parameter is proportional to the rate of atom displacement and is the product of the cross section for producing a primary recoil and the average damage-energy per primary recoil.

Limitations and Discussion

The computer program described here can be applied to most neutron spectra with the following limitations:

- The present omission of (n, γ) limits applications to cases where this reaction is not important.
- The Lindhard expression used for electron-excitation losses is only appropriate for pure metals.
- The nonelastic and Lindhard theories used are invalid for elements lighter than aluminum.

A number of safeguards built into the program protect the user from some of the more common pitfalls. Messages are printed out, and in some cases the calculation is stopped, when the following problems are discovered:

- The material of interest does not match the cross-section and angular distribution input data.
- The defined group boundaries do not fall within the input neutron spectrum.
- The energy entries are not sequential.
- The input data exceeds the dimensioned storage space.
- Neither the angular nor the energy distributions integrate to one.

Also, a warning is printed if the user attempts calculations that are outside of the mass range where the nuclear temperature model is appropriate.

In addition to the above, an option is available for determining the amount of information output. When other input error is suspected, this option allows the user to request the maximum output for checking various stages of the calculation.

Calculations were made for the RTNS-I neutron spectrum on aluminum, titanium, vanadium, iron, nickel, copper, zirconium, niobium, molybdenum, silver, tin, tantalum, tungsten, gold, and lead. Results of these calculations have been published in Ref. 15. For materials that have been calculated by other researchers, the agreement in the calculated damage energy is reasonable.

TECHNICAL NOTES

A Computer-Based Transportable Data Acquisition and Control System *(D. K. Fisher and M. R. Posehn, Materials Engineering Division, and F. L. Sindelar and H. H. Bell, Jr., Nuclear Energy Systems Division)*

As the technology of weapons systems has evolved over the years, so has the variety and sophistication of the physical testing required to evaluate the designs. This testing, in turn, has placed greater demands on the associated data acquisition and control systems. In response to continuing requests for additional data channels, higher data rates, and more sophisticated on-line data processing, the Laboratory has developed a computer-based *t*ransportable *d*ate-*a*cquisition and *c*ontrol (T-DAC) system.

A design team of four engineers used the principles of top-down design[16] to develop the T-DAC system. The computer vendor was selected on the basis of competitive bids submitted in response to a performance specification. Sufficient hardware was purchased to permit future expansion and to allow application software to be developed in FORTRAN, a high-level language. Specialized hardware that could not be purchased as part of the system was developed in-house in parallel with application software. Software development time was minimized by writing application programs in FORTRAN. The use of FORTRAN permitted simultaneous software development on a large-scale time-sharing system and allowed many data processing software modules written for other applications to be utilized for the T-DAC system.

The computer system hardware has an unusual combination of computational power and process interface flexibility. The 16-bit minicomputer system derives its performance from an efficient instruction set, floating-point hardware, large (64 K-word) memory, and a full complement of data-processing peripherals. The latter includes a dual-drive 2.4-megaword disk memory, magnetic tape drive, card-reader, and an electrostatic printer-plotter. The equipment is mounted on castered carts, which are easily moved by hand or fork-lift. It requires no extraordinary cooling and can be set up in less than 30 minutes.

The process interface consists of a variety of analog and digital input/output devices. A wide-range

analog/digital converter, capable of multiplexing up to 128 low-level channels at a burst sampling rate of 20 kHz, is used to support thermal and slow-speed static/dynamic testing. By utilizing the disk memory, sustained sampling rates of 3 kHz are possible. Another analog input/output device, developed for use in shock and vibration testing, acquires up to 16 channels of analog data while simultaneously outputting on 3 others. Synchronous sampling rates to a total of 300 kHz are possible. Higher sampling rates, up to an equivalent of 1 GHz, can be achieved via transient capture devices for a small number of data channels.

The T-DAC system also supports a microprocessor-based two-channel transient recorder. This subsystem, capable of acquiring and displaying raw data in stand-alone operation, can also function as an intelligent data-processing terminal by communicating with the T-DAC computer over dial-up phone lines.

The application software operates in a multitasked environment to perform the functions of data acquisition, reduction, and display. The data-acquisition routines allow the operator to interactively specify and execute a test through a sequence of option menus displayed on a CRT. Once acquired, the data can be manipulated by scaling, nonlinear conversion, integration, spectral analysis, etc. The processed results may be plotted versus time, frequency, one channel versus another, or as a 3-D surface when appropriate. During slow-speed testing the data acquisition, manipulation, and display functions are performed in parallel in order to plot reduced data on a CRT as the experiment progresses.

The hardware and software flexibility of the T-DAC system has lent itself to involvement in a wide variety of testing. Specific applications have included mechanical-impulse response testing (system identification), holographic interferometry, thermal response testing (see Fig. 14), vibration and shock data acquisition/reduction, and vibration shaker control.

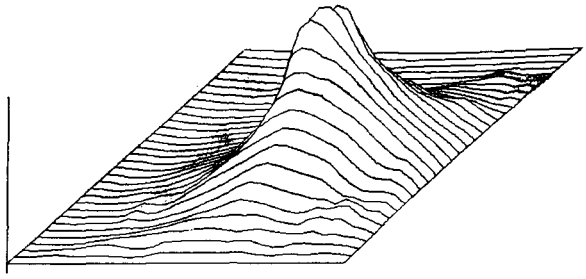

Fig. 14. Three-dimensional temperature surface resulting from exothermic chemical reaction.

Variable Orifice for Differential Pumping in a Vacuum System *(R. Beeman, Research Engineering Division, and S. Brajkovich, Energy Systems Engineering Division)*

In differential pumping, the pumping speed has in the past been controlled by the size of the orifice between the vacuum chamber and the diffusion pump. This fixed orifice is usually in the valve gate of a high-vacuum valve (or in a baffle plate). To change the pumping speed, then, the valve must be removed and another valve with an orifice of a different size must be inserted. This process is time consuming and risks contamination of the system, which would require another pumpdown and bakeout.

We have developed a simple shutter that controls pumping speed without requiring any change in components. The shutter consists of 20 leaves arranged as an iris that opens to a 15-cm-diam orifice or closes to 0.6 cm.

The shutter consists of a mounting ring (Fig. 15a), the leaves, a drive ring, and a drive gear (Fig. 15b). Each leaf is stainless steel with a pivot pin at one end and an offset pin at the other. The leaves are placed in the mounting ring and the drive ring and the drive gear are attached. Rotating the drive gear moves the leaves and changes the orifice size (Fig. 15c).

The complete shutter is stainless steel. Each leaf is made of 0.038-cm stainless steel sheet that is electroetched after assembly to 0.028 cm. At 0.038 cm, the shutter will close down to only 1.9 cm; thinning the leaves provides the extra 1.3-cm closure. We believe that further thinning would cause the leaves to collapse.

The drive mechanism for the shutter is a spur gear rack rolled inside out to form the diameter of the drive ring. It is driven by a spur gear through a vacuum feedthrough in the base plate of the vacuum system. A synchronous motor provides the power. The shutter can be controlled manually, automatically with a thermocouple gage, or by computer.

We have built one of these shutters and used it successfully with a 10-cm diffusion pump system. In this system the pressure is 100 μm in the vacuum chamber and 0.0001 μm at the diffusion pump. The shutter was placed above the cold trap so it could be used for both diffusion pumping and roughing.

Use of a Heavy-Metal Precursor Rod Aides Kinetic-Energy Penetrator *(R. R. Stone, E. R. Hanson, J. L. Knowles, and R. W. Werne, Nuclear Explosives Engineering Division)*

As part of the non-nuclear weapons program, we have investigated a two-stage kinetic-energy penetrator for defeating reinforced concrete structures. A preliminary design has been tested.

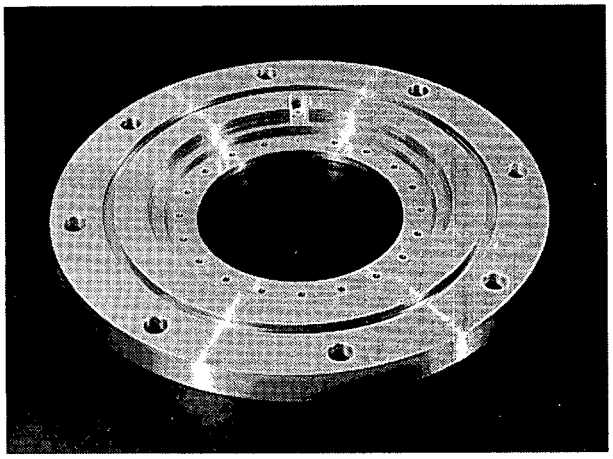

(a)

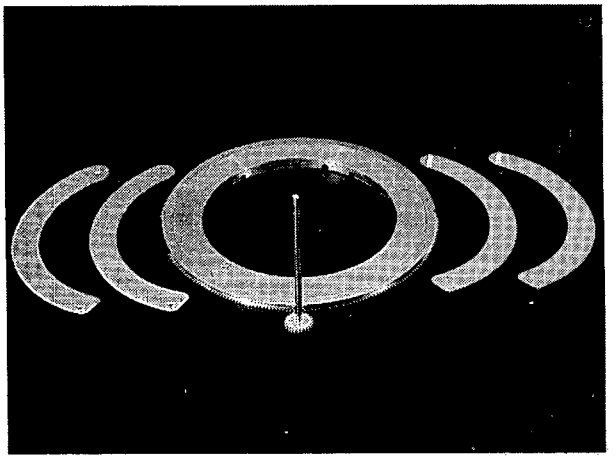

(b)

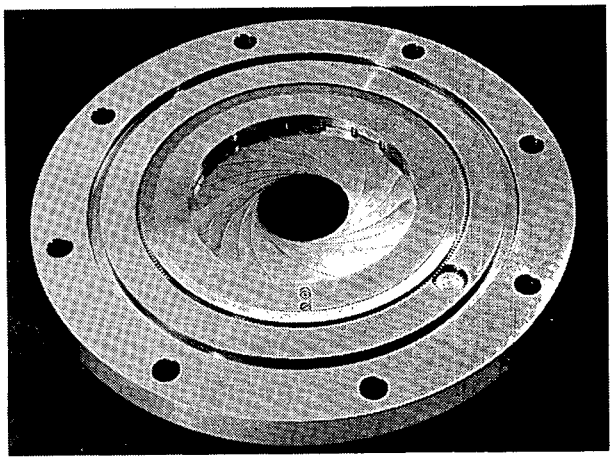

(c)

Fig. 15. The variable orifice. (a) is the mounting ring with an opening 15 cm in diameter. The small inner holes hold the pivot pins of the leaves. (b) shows four of the leaves, the drive gear, and the drive ring with grooves for the offset pins. The movement of the pins in the grooves makes it possible to vary orifice size. (c) shows the drive ring and the drive gear in place, with the shutter partly closed.

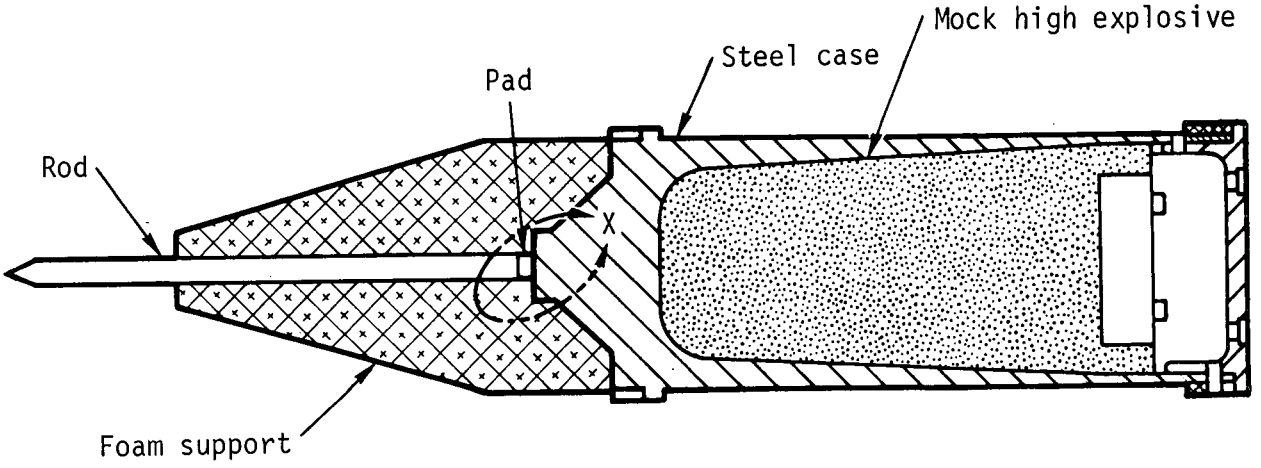

Fig. 16. Assembly drawing of projectile.

This penetrator consists of a steel case loaded with high explosive, preceded by a smaller-diameter tungsten-nickel-iron (W-Fe-Ni) rod (see Fig. 16). The precursor rod fractures and weakens the concrete locally prior to the impact of the warhead. The "softened" concrete will be a less severe environment for the warhead, reducing the probability of premature ignition of the HE. The rod should also minimize chances of the warhead ricocheting off oblique targets.

To test penetration characteristics and structural integrity of the penetrator, two tests were performed. Scaled projectiles were shot from a 155-mm cannon at 488 m/s into 0.76-m-thick reinforced concrete blocks. One projectile had a W-Ni-Fe rod (12.7 mm diameter by 305 mm long) mounted on the front while the other did not.

Results showed that each projectile perforated the target block, making a hole approximately 0.46 m in diameter. These results were inconclusive. However the radial case deformation for the projectile with the rod was only half of that without the rod (see Fig. 17). Thus, the preconditioning of the concrete by the rod reduced the severity of the loading on the projectile.

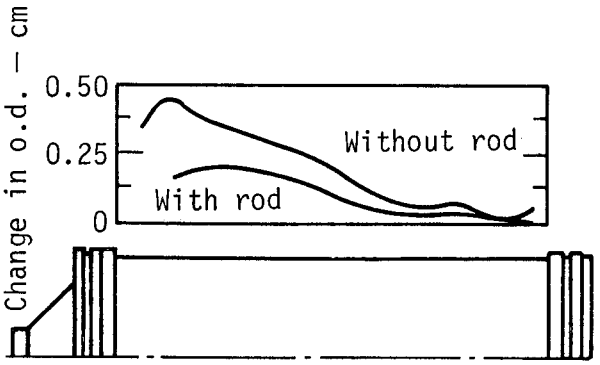

Fig. 17. Radial deformation on projectile shots with and without rod.

PUBLICATION ABSTRACTS

S. Andes, *A One-Dimensional Model for Coaxial Flowing Streams with Condensation,* Lawrence Livermore Laboratory, Rept. UCID-17112 (1976).

An analytical model is developed to identify the basic phenomena present in the high temperature flow (2700 K) of two gaseous coaxial streams. The one-dimensional model potentially has application for design of hardware and test conditions for conducting a laser-isotope-separation feasibility experiment. The processes of interest are those of coupled flow dynamics, liquid condensation of metal vapors, and gaseous diffusion. The stream tubes may initially consist of pure or combinations of an inert carrier – nitrogen, or metal vapor – uranium. A computer code, LISP (Laser Isotope Separation Program), follows from the model. Output from the LISP code is presented for three test cases. They involved stream differences in velocity up to 90,000 mm/s and in temperatures of 1100 K. The rate controlling process for the cases sited was found to be diffusion. However, condensation was present. Further use of the LISP code should continue to give a better understanding into the coupled processes of diffusion, condensation, and flow dynamics.

D. R. Roach and H. S. Freynik, Jr., *Evaluation of the Kulite Semiconductor Strain Gage, Model M(6) EP-120-500W, Spotwelded to P-110 Pipe Material,* Lawrence Livermore Laboratory, Rept. UCID-17165 (1976).

The Kulite dual-element, semiconductor strain gage, weldable model M(6)-EP-120-500W, was evaluated in laboratory tests under simulated Nevada Test Site conditions. Two gages were installed on P-110 line-of-sight pipe material. Tension was applied to the test samples to 50% of yield (about 2000 microstrain). Immediately following, compression was applied to 100% of yield (about 6000 microstrain). The Kulite gages were powered by a dual constant current signal conditioner, measurements obtained with metal foil gages served as reference standards for the Kulite strain gage measurements.

The output voltages of the Kulite gages were relatively linear from zero to +2000 microstrain and in the subsequent compression to -2500 microstrain. Below -2500 microstrain, the output voltages from the Kulite gages became decidedly nonlinear and also differed significantly from each other. We feel that the gage spotwelds were failing at strains below -2500 microstrain and consequently that data obtained below this level are not reliable enough to calculate pipe forces. The stated gage factor (Kulite factory) of 220 is about 33% higher in tension than the measured gage factor and about 15% higher in compression.

Adhesive-bonded, metal foil strain gages are recommended for reliable pipe force measurements on future Nevada Test Site events. Metal foil gages consistently are linear and reliably measure strains in excess of ±10,000 microstrain.

C. W. Jensen and C. E. Hugenberger, *Technology training Program: Transferring the Technology of Welding and Bonding – Hands-On Courses at LLL Make It Possible*, Lawrence Livermore Laboratory, Rept. UCID-17226 (1976).

This report, the second in a new series of technology training reports, outlines the Technology Training Program approach to the transfer of unclassified technologies from LLL to public use. A detailed description of the "Welding and Bonding Technology" courses given in the Spring of 1976 is presented as well as student and administrative evaluations of the program.

D. F. Alves and G. L. Goudreau, *Structural Response Calculations for a Reverse Ballistics Test of an Earth Penetrator*, Lawrence Livermore Laboratory, Rept. UCID-17241 (1976).

A dynamic response calculation has been performed on a half-scale earth penetrator to be tested on a reverse ballistics test in August 1976. In this test, a 36-cm-diameter sandstone target is fired at the EP at 549 m/s at normal impact. Several other calculators are independently attempting to predict the internal structural response of the penetrator based on the loading conditions predicted by California Research and Technology (CRT), which modeled a rigid body penetrating the sandstone media.

Basically two types of calculations were made. The first utilized an axisymmetric, finite element code DTVIS2 in the dynamic mode and with materials having linear elastic properties. CRT's radial and axial force histories were smoothed to eliminate grid encounter frequency and applied to the nodal points along the nose of the penetrator. Given these inputs DTVIS2 then calculated the internal dynamic response. Secondly, SAP4, a structural analysis code, is utilized to calculate axial frequencies and mode shapes of the structure. A special one-dimensional display facilitates interpretation of the mode shape. DTVIS2 and SAP4 use a common mesh description.

Special considerations in the calculation are the assessment of the effect of gaps and preload and the internal axial sliding of components.

M. D. Meyer, *Holographic Determination of the Yield Strength of a Welded Stainless Steel Pressure Vessel*, Lawrence Livermore Laboratory, Rept. UCID-17247 (1976).

A part of the Metallurgy Division's Advanced Steel Technology Program involves evaluation of stainless steels used in pressure vessels. In particular, the strength and toughness of a high-energy-rate-formed (HERF'ed) stainless steel, as influenced by the heat input from a variety of welds, are being measured. Using holographic interferometry, we have examined a welded spherical pressure vessel constructed from HERF'ed stainless steel with a composition of 21% Cr, 6% Ni, 9% MN, 0.23% N, balance Fe. We found that the yield strength in the heat-effected zone was about 300 MPa, but was less than the base material.

K. D. Pimental, *Toward a Mathematical Theory of Environmental Monitoring: The Infrequent Sampling Problem*, Lawrence Livermore Laboratory, Rept. UCRL-51837 (1976).

An environmental monitor can be defined as a system that estimates environmental pollutant levels throughout an environmental region for all times in a specified time interval, using measurement data taken only at discrete locations and at discrete times. Our goal in this study was to find an optimal environmental monitoring program. We considered the numbers and types of measurement devices to use, where to locate them, and measurement timing. An optimal monitoring program would minimize the total cost of taking measurements while keeping errors in the pollutant estimates below an allowable level.

We considered optimal solutions to two distinct monitoring problems: the first for environmental feedback control applications, the second for detecting violations of pollutant limits. The structure of an optimal solution to these monitoring problems is straightforward. First, a general form of the linear, distributed-parameter equation-of-pollutant transport is presented. For mathematical simplicity, the scope of transport mechanisms considered is limited to problems in diffusion with scavenging and stochastic point sources. The distributed parameter model for diffusive transport is then treated with the method of separation of variables to obtain a set of decoupled stochastic first-order, ordinary differential-state equations. Techniques of optimal estimation theory are then applied to the system of modal state equations, yielding a set of matrix-estimation error-covariance equations which are then solved as discrete matrix recurrences. The solutions to the covariance matrix recurrence relations are used in accuracy measures for the resulting pollutant estimates in the synthesis of optimal environmental monitoring systems.

The main results are associated with the infrequent sampling problem. If the estimation error constraints imposed upon the monitor are sufficiently lax, the solution for the optimal monitoring program results

in relatively long times between required measurements. This leads to drastic simplifications in solving the problems of optimally designing and sequencing the measurements, where only certain terms in the solutions of the estimation equations are found to affect the solution for large time. Furthermore, when the measurement error and source statistics are constant, the optimal solution is independent of time so that it may be precomputed offline.

The dominance of certain asymptotic terms has potential for future application in more complex environmental pollutant transport problems. Although the results are developed for the case of diffusion where solutions exist in separated variables, they apply to more general problems as well, including combined diffusion and advection.

Owing to the ease in their interpretation, numerical experiments for one-dimensional diffusive systems are included to illustrate the main results, though all the results are shown to generalize to the three-dimensional case. Considerable use of graphical computer output is made which clearly exhibits the features of the infrequent sampling problem. We give extensive references relevant to the optimal monitoring problem.

G. E. Cummings and W. W. Feng, *Modeling Considerations in the Vibration Analysis of Reactor Internals*, Lawrence Livermore Laboratory, Rept. UCRL-52023 (1976).

We completed a study for the Nuclear Regulatory Commission to determine the types of analysis and testing needed to characterize the effect of coolant flow on the internal structures of a nuclear power reactor. Using finite-element structural response codes, we identified response modes and natural frequencies of the reactor core support barrel and a fuel assembly. We looked at the effect of coolant on these natural frequencies, using the "added-mass" technique, and we explored the accuracy of lumped-mass models used to define the natural frequencies of the fuel assembly. We found that including the coolant and the surrounding structures reduced the natural frequencies of the core support barrel by greater than 50%. We also found that lumped-mass models using four to eight lumps are adequate for computing the natural frequencies of the fuel assembly.

P. A. House, *Helical-Rotor Expander Applications for Geothermal Energy Conversion*, Lawrence Livermore Laboratory, Rept. UCRL-52043 (1976).

The helical-rotor expander is one of numerous candidates for the direct "total flow" expansion of geothermal fluids. The potential exists for expansion efficiencies as high as 70%. Engine efficiencies will generally be below 70% because of an expansion-ratio limitation of 15 and a maximum pressure differential of 110 psi.

Single-stage expansion of self-pumped geothermal fluids from reservoirs at 350 to 752°F gives engine efficiencies in the range from 57.3 to 43.1%. Calculated rotor diameters range from 10.5 to 41.6 ft for a range of 5 to 40 MW.

Two-stage expansion of fluid from the 572°F reservoir gives an engine efficiency of 62.3% and a 21% reduction in the diameter of the larger rotor. Rotor diameters can be held to more reasonable sizes by using the expander in combination with a vapor turbine. For the expansion of reservoir fluid at 572°F (360 psia at the wellhead with 18.9% quality) to helical-rotor-expander exhaust pressures ranging from 66 to 14.7 psia, calculations give rotor diameters of 4 to 8.5 ft for a 40-MW combined system power output. Corresponding system engine efficiencies vary from 58.7 to 55.3%.

The impulse contribution to the total work of the expander ranges from 7.7 to 8.5% when 572°F reservoir fluid is expanded to backpressures from 1.69 to 14.7 psia, respectively.

The better applications for the helical-rotor expander are for noncondensing, low-power-output uses or in a hybrid system with helical-rotor exhaust pressures above 1 atm.

J. O. Hallquist, *A Procedure for the Solution of Finite-Deformation Contact-Impact Problems by the Finite Element Method*, Lawrence Livermore Laboratory, Rept. UCRL-52066 (1976).

In this report, a numerical procedure is presented for solving the finite-deformation dynamic contact-impact problems by the finite element method. After impact, penetration is precluded by constraint conditions that are imposed by a transformation of the generalized displacements in the equations of motion. Either friction or frictionless interface conditions can be assumed along the contact surface.

Five numerical examples are provided to demonstrate the accuracy and the flexibility of the method.

B. O. Sellick, *Formation and Evaluation of Convex-Curved Crystals of Lithium Fluoride for Use in Analyzing X-ray Spectra*, Lawrence Livermore Laboratory, Rept. UCRL-52086 (1976).

Lithium fluoride as received from the vendor in boule form is 38 X 38 X 13 mm thick. This block is cleaved to wafers of the desired thickness, x-ray-evaluated for "d" spacing and greatest intensity, bent (plastically deformed) to the required radius, and then acid-etched to remove foreign material. The

diffraction and dispersion characteristics of a wafer are analyzed using well-collimated tungsten x rays that strike the crystal and are diffracted onto no-screen x-ray film. If the crystal is satisfactory, it is mounted in a spectrogoniometer and rotated through an x-ray beam while a detector is set at the optimized angle for the diffracted x rays. The average intensity across the length of the crystal is recorded by multichannel scaling. Any inperfections appear as peaks or dips compared to the average intensity.

The crystal next goes to a 10-channel, filter-fluorescer x-ray unit that compares zero-order intensity to diffracted Kα and Kβ intensity. Counts for 100-s intervals are taken in groups of three and averaged. Correction factors for instrument geometry, air, pinhole diameter at zero order, Kα-Kβ, barometric pressure, temperature, etc., are added to the efficiency calculations to obtain the crystal efficiency (ϵ) vs keV data. The crystal is mounted in the spectrograph or spectrometer and calibrated to either the detector or films plane by using direct radiation with proper x-ray filters or absorbers. The crystal is then ready for use.

B. O. Sellick, *Modification of the X-ray Diffraction Efficiency of Lithium Fluoride Crystals by Surface Treatment*, Lawrence Livermore Laboratory, Rept. UCRL-52087 (1976).

Convex-curved crystals of lithium fluoride demonstrate good dispersion and efficiency when used in reflection of x-ray spectral analysis. The crystals are stable and reasonably unaffected by harsh environments. In addition, they are mechanically strong, easily cleavable or machinable, and plastically deformable with heat.

In the present study, flat crystal wafers were left either clear as cleaved or were subjected to surface treatment by sandblasting or lapping. Some wafers were then bent in a press mold to obtain convex-curved crystals of differing radii. The diffraction efficiency data presented show how surface treatment affects the efficiency of these various crystals when used as x-ray diffracting agents.

D. J. Bander and J. D. Lee, *The Potential for Fissile Breeding with the Fusion-Fission Hybrid Reactor*, Lawrence Livermore Laboratory, Rept. UCRL-77887 (1976). Presented at the American Nuclear Society Summer Meeting, Toronto, Canada, June 14, 1976.

As part of the Mirror Hybrid Program for FY 1976, we have developed a system model of the mirror hybrid reactor, which has been used to optimize the reactor design for fissible breeding. The objective of the optimization has been to minimize the cost of producing fissile material for consumption in fission power reactors. We have considered two types of blankets for the hybrid, the first containing ^{238}U and producing ^{239}Pu, and the second containing ^{232}Th and producing ^{233}U. Our projected costs for fissile material from the optimized hybrid configuration is about \$50/g for ^{239}Pu and about \$125/g for ^{233}U.

B. Myers, R. Landingham, P. Mohr, and R. Taylor, *A Topping Cycle for Coal-Fueled Electric Power Plants Using the Ceramic Helical Expander*, Lawrence Livermore Laboratory, Rept. UCRL-77905 (1976). Submitted to the EPA-ERDA Symposium on the Environment and Energy Conservation, Denver, Colorado, November 3-6, 1975.

We advocate ceramic helical expanders as the work output element in a 2500°F direct coal-fired Brayton topping cycle for central power station application. When combined with a standard steam-electric power plant cycle, such a cycle could result in an overall thermal conversion efficiency in excess of 50%. We enumerate the performance, coal tolerance, and system-development-time advantages of the ceramic helical expander approach. We provide a perspective on the choice of design and materials.

A preliminary consideration of physical properties, economic questions, and service experience has led us to a preference for the silicon nitride and silicon carbide family of materials. A program to confirm the performance and coal tolerance aspects of a ceramic helical expander system is planned.

J. O. Halliquist and W. W. Feng, *On the Explicit Finite Element Formulation of the Dynamic Contact Problem of Hyperelastic Membranes*, Lawrence Livermore Laboratory, Rept. UCRL-78055 (1976). Submitted to the 13th Annual Meeting of Engineering Science, Inc., Hampton, Virginia November 1-3, 1976.

Contact-impact problems involving finite deformation axisymmetric membranes are solved by the finite element method with explicit time integration. The formulation of the membrane element and the contact constraint conditions are discussed in this paper. The hyperelastic, compressible Blatz and Ko material is used to model the material properties of the membrane. Two example problems are presented.

D. E. Maiden, *Numerical Simulation of Tornado Wind Loading on Structures*, Lawrence Livermore Laboratory, Rept. UCRL-78073 (1976). Submitted to the 13th Annual Meeting of the Society of Engineering Science, Inc., Hampton, Virginia, November 1-3, 1976.

A numerical simulation of a tornado interacting with a building was undertaken in order to compare the pressures due to a rotational unsteady wind with that due to steady straight winds currently used in design

of nuclear facilities. The numerical simulations were performed on a two-dimensional compressible hydrodynamics code. Calculated pressure profiles for a typical building is then subjected to a tornado wind field and the results are compared with current quasi-steady design calculations. The analysis indicates that current design practices are conservative.

M. A. Hamstad, R. Bianchetti, and A. K. Mikherjee, *A Correlation Between Acoustic Emission and the Fracture Toughness of 2124-T851 Aluminum*, Lawrence Livermore Laboratory, Rept. UCRL-78151 (1976). Submitted to *Engineering Fracture Mechanics.*

The paper reports on an experimental study of the possible application of acoustic emission as an inspection technique, to determine whether 2124-T851 aluminum plate meets certain, minimum, fracture toughness specifications. Unflawed specimens, taken in the three principal directions, from three separate plates are tested in compression and tension. The true-mean-square or the root-mean-square voltage of the continuous acoustic emission generated during the tests is recorded as a function of specimen strain. The acoustic emission, chemical analysis, fracture surfaces, and large (1-20 μm) second-phase particles are studied in relation to fracture toughness. Results indicate that the generated acoustic emission from a longitudinal compression test, long-transverse tension test, and short-transverse tension test all correlate with change in plate fracture toughness. Based on the experimental results, the monitoring of acoustic emission during relatively simple tension or compression tests of aluminum may be useful in checking whether the material meets a fracture toughness specification. Also, the results indicate that acoustic emission is useful in studies to develop fracture toughness models.

M. A. Hamstad and T. T. Chiao, *Structural Integrity of Fiber/Epoxy Vessels by Acoustic Emission: Some Experimental Considerations*, Lawrence Livermore Laboratory, Rept. UCRL-78198 (1976). Submitted to *SAMPE Quarterly.*

The application of acoustic emission to the prediction of the burst pressure of pressure vessels wound with organic fiber/epoxy filament has been studied. Experimental aspects of this work included determination of longitudinal and shear velocities, propagation signal losses, resonant vs non-resonant acoustic emission transducers, pressure vessels of different sizes and thicknesses, different epoxy systems, and frequency spectrum analysis. The central conclusion is that the acoustic emission system should be operated with a relatively low frequency bandpass to avoid large propagation signal losses.

S. S. Glaros, P. Baker, and D. Milam, *Dielectric Coatings and Metal Substrates*, Lawrence Livermore Laboratory, Rept. UCRL-78249 (1976). Submitted to Proceedings of 1976 Symposium on Optical Materials for High Power Lasers, Boulder, Colorado, July 15-17, 1976.

Large aperture, beryllium-subtrate-based mirrors have been used to focus high intensity pulsed laser beams. Finished surfaces have high reflectivity, low-wavefront distortion, and high-laser damage thresholds. This paper describes the development of a series of metallic coatings, surface finishing techniques and dielectric overcoatings to meet specified performance requirements. Beryllium substrates were coated with copper, diamond machined to within 5 micro-inches to final contour, nickel plated and abrasively figured to final contour. Bond strengths for several bonding processes will be presented. Dielectric overcoatings were deposited on finished multimetalic substrates to increase both reflectivity and the damage thresholds. Coatings were deposited using both high and low temperature processes which induce varying stresses in the finished coating substrate system. Data will be presented to show the evolution of wavefront distortion, reflectivity, and damage thresholds throughout the many steps involved in fabrication.

A. H. Cassell, *Continuing Education at the Lawrence Livermore Laboratory*, Lawrence Livermore Laboratory, Rept. UCRL-78270 (1976).

This paper discusses the philosophy, organization, and rationale of the Continuing Education program for engineers and scientists at the Lawrence Livermore Laboratory in Livermore, CA. The importance of diversified offerings designed to fit the needs of the individual is stressed, as is the recognition that continuing education is not necessarily confined to the traditional teacher-student relationship. The impact of the video cassette player is discussed for employees unable to meet rigid class schedules, as are the television links to the major universities in Northern California.

D. E. Maiden and A. M. Winslow, *A Simple Analysis of Large Deflections and Rupture of Circular Plates Under Impulsive Loading*, Lawrence Livermore Laboratory, Rept. UCRL-78279 (1976). Submitted to *Journal of Applied Physics.*

Simple formulas for large deflections and rupture of impulsively loaded simply supported and clamped circular plates are derived in terms of impulse, plate geometry, and material properties. Elastic and plastic

bending and membrane effects are included, as well as strain hardening and strain rate dependence.

Since analytical and experimental results reveal that the final deformed shapes are almost identical for all plates irrespective of thickness, diameter, and load, the deflected shape, i.e., a cone with a rounded tip, is assumed a priori. The stresses and strains for the plate are analyzed on the basis of the deformation theory of plasticity using the von Mises yield condition and the Prandtl-Reuss flow rule. The limiting deflections are obtained by equating the kinetic and strain energies.

Predictions from this model show clearly where bending and membrane effects are important. The results are verified by experimental measurements and by calculations with two-dimensional finite difference and finite element codes.

N. J. Brown, *Axisymmetric Aspheric Lens Figuring for the Small Shop*, Lawrence Livermore Laboratory, Rept. UCRL-78320 (1976). Submitted to *Optical Engineering.*

This paper presents a method for predicting wear patterns for aspheric axisymmetric lens figuring employing simple graphic and algebraic computation. It is written for the small shop optician rather than the academician.

F. Cooke, N. Brown, and E. Prochnow, *Annular Lapping of Precision Optical Flatware*, Lawrence Livermore Laboratory, Rept. UCRL-78321 (1976). Submitted to *Optical Engineering.*

In recent years, the continuously dressed flat annular machines widely used for flat grinding have been adapted to polishing ultra-flat optical surfaces for interferometry and laser applications. This paper describes these machines and the theory and practice of their operation to achieve peak to valley flatness better than 1/10 wavelength in the visible.

R. H. Bulmer, M. O. Calderon, D. N. Cornish, T. A. Kozman, and S. J. Sackett, *The MX Magnet System*, Lawrence Livermore Laboratory, Rept. UCRL-78335 (1976). Submitted to the 1976 Applied Superconductivity Conference, Stanford University, Stanford, California, August 17-20, 1976.

The Lawrence Livermore Laboratory has put forward proposals for building a large mirror fusion experiment called MX (Mirror Experiment). This machine is designed to advance both the physics of mirror systems and the technologies which will be required on future machines such as FERF (Fusion Engineering Research Facility) and reactors. One such technology to benefit is superconductivity, since the confining field will be generated by two large NbTi Yin-Yang shaped coils. the maximum field at the conductor is 7.5 T and the total stored energy is 500 MJ. The paper gives details of the magnet system conceptual design including the design philosophy of the superconductor and the structure to restrain the very large electromagnetic forces.

D. L. Bernreuter, *Estimates of the Epicentral Ground Motion in the Central and Eastern United States*, Lawrence Livermore Laboratory, Rept. UCRL-78369 (1976). Submitted to the Sixth World Earthquake Conference, New Delhi, India, January 10-14, 1977.

In this paper seismic ground motion from earthquakes in the central U.S. recorded at regional distances is used as a basis to make estimates of the strong ground motion that could be expected from future earthquakes in the central U.S.. The method used to back extrapolate the data into the near field is shown to be valid by use of data from earthquakes and underground nuclear explosions. The results of this study show that the estimated peak accelerations in the epicentral region are similar to that observed elsewhere throughout the world. The differences between these results and the lower values predicted by Nuttli are also discussed.

R. G. Dong and F. J. Tokarz, *Seismic Effects on Modularized Spent Fuel Storage Facilities*, Lawrence Livermore Laboratory, Rept. UCRL-78370 (1976). Submitted to the Sixth World Earthquake Conference, New Delhi, India, January 10-14, 1977.

Large pools are being considered to provide additional storage capacity for spent fuel from nuclear power plants. Because of the large size modularization of the pool into cells would enhance operational safety and convenience in terms of isolating trouble spots and performing localized clean-up. However, the effects of modularization on earthquake resistant was not clear. An investigation of these effects was made and the results are presented. Our findings indicate modularization may or may not be advantageous in terms of structural loads depending on the pool configuration and installation.

L. H. Wight, *Soil-Structure Interaction in Nuclear Power Plants: A Comparison of Methods*, Lawrence Livermore Laboratory, Rept. UCRL-78371 (1976). Submitted to the Sixth World Earthquake Conference, New Delhi, India, January 10-14, 1977.

We performed an extensive parametric survey to analyze the differences between two methods of calculating soil-stucture interaction. One method

involves discretizing the soil-structure system and solving for the complete response with the LUSH computer code. The other method solves for the lumped mass structure response with Whitman soil springs. Twelve soil-structure interaction problems are solved by each of these methods. Representative results are presented and discussed.

R. C. Murray and F. J. Tokarz, *Seismic Evaluation of Critical Facilities at the Lawrence Livermore Laboratory*, Rept. UCRL-78374 (1976). Submitted to the Sixth World Earthquake Conference, New Delhi, India, January 10-14, 1977.

The performance of critical facilities at the Lawrence Livermore Laboratory is being evaluated for severe earthquake loading. Facilities at Livermore, Site-300, and the Nevada Test Site are included in this study. These facilities are identified, the seismic criteria used for the analysis are indicated, the various methods used for structural analysis are discussed, and a summary of the result of facilities analyzed to date are presented.

D. C. Thompson, *Theoretical Tool Movement Required to Diamond Turn and Off-Axis Paraboloids on Axis*, Lawrence Livermore Laboratory, Rept. UCRL-78411 (1976). Submitted to Advances in Precision Machining of Optics 20th Technical Symposium, Society of Photo-Optical Instrumentation Engineers, San Diego, Cal., August, 1976.

Current techniques for manufacturing off-axis paraboloids are both expensive and insufficiently accurate. An alternative method, turning the workpiece about its axis on a diamond-turning machine, is presented, and the equations describing the necessary tool movement are derived. A discussion of a particular case suggests that the proposed technique is feasible.

H. Lambert, *Fault Trees for Location of Sensors in Chemical Processing Systems*, Lawrence Livermore Laboratory, Rept. UCRL-78442 (1976). Submitted to American Institute of Chemical Engineers, 69th Annual Meeting, Chicago, Ill., December, 1976.

This concepts of probabilistic importance within the context of fault tree analysis is presented. On the basis of probabilistic importance of events in fault trees, it is shown how to optimally locate sensors in a system. Two kinds of sensors are described: preventive sensors to detect early failures of critical redundant components; diagnostic sensors to detect potentially catastrophic system fault conditions. A SO_2-O_2 conversion process is chosen as an example to illustrate the methods that are presented.

D. W. Deiss, *Multifilament NB_3Sn Conductors: Progress and Prospect*, Lawrence Livermore Laboratory, Rept. UCRL-78463 (1976). Published in the Proceedings of the Applied Superconductivity Conference, Palo Alto, California, August 17-20, 1976.

Multifilament NB_3 conductors are now at the stage where several coils have been constructed and various types of material are available commercially from several suppliers. Even so, some questions remain with regard to the reliable use of this material, particularly in large-scale systems. The initial portion of this paper covers the main features of past work as they relate to the present situation. In the latter part, those areas where major uncertainties remain are described along with current projected work in these areas.

T. T. Saito and J. Arnold, *Metrology of Diamond-Turned Toric Resonator Component*, Lawrence Livermore Laboratory, Rept. UCRL-78494 (1976). Submitted to the Advances in Precision Machining of Optics Symposium, S.P.I.E., San Diego, California, August 26-27, 1976.

We describe the set up and measurement techniques to evaluate a diamond-turned 300-mm-diameter copper toroid. A single-beam interferometer, rotary table, and Moore measuring machine were used to measure the circular flatness of 0.63-μm- and 30-nm-rms figure deviation. A computer program was used to evaluate the figure and absolute average slope error of 12 μrad.

R. W. Werne and J. M. Kelley, *A Dislocation Theory of Isotrophic Polycrystalline Plasticity*, Lawrence Livermore Laboratory, Rept. UCRL-78572 (1976). Submitted to the *Journal of the Mechanics and Physics of Solids.*

A theory of polycrystalline plasticity is developed in which the polycrystalline solid is modeled as an isotropic continuum. The rate of plastic deformation tensor is shown to be a function of the mobile dislocation density and the dislocation velocity vector summed over all active glide planes. A representation theorem for isotropic functions is used to express the dislocation velocity vector in terms of the stress tensor and the normal vector to the dislocation glide plane. The condition of plastic incompressibility yields the fact that the dislocation glide planes are the octahedral shear planes of the stress tensor. As a special case the rate of plastic deformation tensor reduces to a relation analogous to the Prandtl-Reuss flow rule.

A. H. Cassell and R. J. Wasley, *Please Say Something for the Kids in Algebra, Mr. Smith*, Lawrence

Livermore Laboratory, Rept. UCRL-78578 (1976). Submitted to *Engineering Education Journal.*

This paper examines the advantages of melding the educational system more closely with the industrial and manufacturing areas in which most graduates will ultimately work and stresses the problem of the slow divergence of education from the real world of work. The paper further describes some of the activities of the Lawrence Livermore Laboratory in "boarding around" (bringing teachers to the laboratory) and offers some suggestions for other industrial and manufacturing agencies.

T. H. Johnson, J. Killeen, O. A. Anderson, and M. E. Resnink, *Guiding-Center Simulation of Toriodal Plasmas*, Lawrence Livermore Laboratory, Rept. UCRL-78597 (1976). Submitted to the *Journal of Computational Physics.*

A new computer simulation method for axisymmetric toroidal plasmas is developed. The method comprises two separate physical models representing different components of an experimental plasma. The first model is an MHD fluid equilibrium representation; the technique devised for the solution of this equilibrium is faster than any currently in common use. The second model is a macroparticle representation which uses guiding-center formalism for the particles' velocities and position; consequently, the timestep used by this model may be many times longer than those possible for conventional macroparticle simulations. A new computer code, GUIDON, which incorporates these models with solution for self-consistent magnetic fields, is presented. Special features of the guiding-center model are discussed in detail. Results of simulations using GUIDON are also presented.

R. P. Freis, C. W. Hartman, J. Killeen, A. A. Mirin, and M. F. Uman, *Calculations of Combined Stellarator-Multipole Toroidal Magnetic Field Configurations*, Lawrence Livermore Laboratory, Rept. UCRL-78598 (1976). Submitted to the *Journal of Nuclear Fusion*.

Numerical computation of closed, vacuum magnetic field configurations is discussed. Comparisons are made of several representations of the fields of various stellarator systems. The calculations are extended to evaluate hybrid configurations which incorporate both stellarator-like fields and axisymmetric fields. Results are given to show that large shear, large rotational transform, and large magnetic well depth can be obtained.

References

1. G. E. Sommargren, *Precision Double-Exposure Holographic Interferometry*, Lawrence Livermore Laboratory, Rept. UCRL-78300 (1976).
2. R. G. Dong, *Water Response in Large Pools Under Earthquake-like Grounds Motions*, Lawrence Livermore Laboratory, Rept. UCRL-78489 (1976).
3. G. W. Housner, "Dynamic Pressures on Accelerated Fluid Containers," *Bulletin of the Seismological Society of America*, **47** (1), 15 (1975).
4. H. N. Abramson and G. E. Randsleben, Jr., *Some Comparisons of Sloshing Behavior in Cylindrical Tanks with Flat and Conical Bottoms*, Southwest Research Institute, San Antonio, Texas, Technical Rept. 4, SwRI Project 43-768-2 (1959).
5. H. N. Abramson, *The Dynamic Behavior of Liquids in Moving Containers*, National Aeronautics of Space Administration, Rept. NASA SP-106 (1966).
6. D. D. Kana and F. T. Dodge, *Design Support Modeling of Liquid Slosh in Storage Tanks Subject to Seismic Excitation*, presented at the Second ASCE Speciality Conference on Structural Design of Nuclear Plants Facilities, New Orleans, La., Dec., 1975.
7. W. J. Comfort, T. W. Alger, W. H. Giedt, and C. T. Crowe, *Calculation of Two-Phase Dispersed Droplet-in-Vapor Flows Including Normal Shock Waves*, Lawrence Livermore Laboratory, Rept. UCRL-78426 (1976).
8. S. L. Soo, *Fluid Dynamics of Multiphase Systems*, (Blaisdell Publishing Company, Waltham Massachusetts, 1967).
9. R. W. MacCormach, *The Effect of Viscosity in Hypervelocity Impact Cratering*, AIAA Paper 69-354.
10. S. Sundstrom, Numerical Mathematics Seminar, Lawrence Livermore Laboratory, December 11, 1975.
11. T. W. Alger, *Shock Capturing Technique of a Quasi-One-Dimensional Nozzle Flow*, Lawrence Livermore Laboratory, Rept. UCRL-77573 (1975).
12. H. Weiss, *Geothermal Two-Phase Flow Test Facility*, Lawrence Livermore Laboratory, Rept. UCRL-76409 (1975).
13. T. W. Alger, "The Performance Of Two-Phase Nozzles For Total Flow Geothermal Impulse Turbines," in *Proc. of the Second United Nations Symposium On The Development And Use Of Geothermal Resources*, (San Francisco, 1975).
14. H. A. Warda, F. R. Mobbs, and B. N. Cole, *Gas Solids Flow In Supersonic Nozzles*, ASME Paper No. 75-WA/HT-35 (1975).
15. C. M. Logan and E. W. Russell, *Radiation Damage at the Rotating Target Neutron Source (RTNS-I) Facility of Lawrence Livermore Laboratory*, Lawrence Livermore Laboratory, Rept. UCRL-52093 (1976).
16. K. D. Fisher and F. W. Hollowy, *Process-Control Computer System Development: A Philosophy*, Lawrence Livermore Laboratory, Rept. UCRL-76112 (1974).

MBB/edas/vt/lmc